Article

Active Touch and Self-Motion Encoding by Merkel Cell-Associated Afferents

Highlights

- Recordings from identified Merkel afferents during active touch

- Touch and position (phase within whisk cycle) are both encoded

- A simple mechanical model accounts for Merkel afferent spiking

- Phase coding depends on both external and internal forces

Authors

Kyle S. Severson, Duo Xu,
Margaret Van de Loo, Ling Bai,
David D. Ginty, Daniel H. O'Connor

Correspondence

dan.oconnor@jhmi.edu

In Brief

Severson, Xu et al. recorded from identified Merkel cell-associated and other primary afferents in behaving mice. Surprisingly, these mechanoreceptor neurons encoded not only the properties of touched objects, but also whisker position, suggesting a dual role in touch and proprioception.

CellPress

Neuron

Article

CellPress

Active Touch and Self-Motion Encoding by Merkel Cell-Associated Afferents

Kyle S. Severson,[1,3,4] Duo Xu,[1,3,4] Margaret Van de Loo,[1] Ling Bai,[2,3] David D. Ginty,[2] and Daniel H. O'Connor[1,5,*]

[1]Kavli Neuroscience Discovery Institute, Brain Science Institute, The Solomon H. Snyder Department of Neuroscience, The Johns Hopkins University School of Medicine, Baltimore, MD 21205, USA
[2]Department of Neurobiology, Howard Hughes Medical Institute, Harvard Medical School, 220 Longwood Avenue, Boston, MA 02115, USA
[3]Neuroscience Training Program, The Johns Hopkins University School of Medicine, Baltimore, MD 21205, USA
[4]These authors contributed equally
[5]Lead Contact
*Correspondence: dan.oconnor@jhmi.edu
http://dx.doi.org/10.1016/j.neuron.2017.03.045

SUMMARY

Touch perception depends on integrating signals from multiple types of peripheral mechanoreceptors. Merkel-cell associated afferents are thought to play a major role in form perception by encoding surface features of touched objects. However, activity of Merkel afferents during active touch has not been directly measured. Here, we show that Merkel and unidentified slowly adapting afferents in the whisker system of behaving mice respond to both self-motion and active touch. Touch responses were dominated by sensitivity to bending moment (torque) at the base of the whisker and its rate of change and largely explained by a simple mechanical model. Self-motion responses encoded whisker position within a whisk cycle (phase), not absolute whisker angle, and arose from stresses reflecting whisker inertia and activity of specific muscles. Thus, Merkel afferents send to the brain multiplexed information about whisker position and surface features, suggesting that proprioception and touch converge at the earliest neural level.

INTRODUCTION

The stimulus sensitivities of multiple types of low-threshold mechanoreceptors have been described in several mammalian systems, including the glabrous skin of the primate fingertip and mouse hairy skin (Abraira and Ginty, 2013; Johnson, 2001). In the fingertip and hairy skin, decades of work have characterized responses of slowly adapting (SA) type 1 afferents, which correspond to large-diameter nerve fibers that associate with Merkel cells in the skin (Iggo and Muir, 1969; Woodbury and Koerber, 2007). Recent work has shown that mechanical activation of Piezo channels drives spiking in both Merkel cells and their afferents (Ikeda et al., 2014; Maksimovic et al., 2014; Ranade et al., 2014; Woo et al., 2014), and that Merkel cells synaptically excite their afferents (Chang et al., 2016; Maksimovic et al., 2014).

Merkel cell-associated afferents (Merkel afferents) are thought to play a crucial role in perception of spatial form due to their small, densely packed receptive fields and their high-fidelity responses to the surface properties of touched objects (Johnson, 2001; Johnson and Hsiao, 1992; Johnson et al., 2000). However, Merkel afferent activity has been studied almost entirely with passively applied stimuli. Touch is an active sense and typically occurs in the context of self-generated motions, where mechanics that govern interactions with the world can be quite different. The role of Merkel afferents in active touch is unknown.

While humans explore the tactile environment largely through hand movements, mice seek out tactile information by sweeping their whiskers through the space surrounding their heads. The rodent whisker system is a powerful model for sensory-motor integration (Diamond and Arabzadeh, 2013; Diamond et al., 2008; Kleinfeld and Deschênes, 2011; Maravall and Diamond, 2014), due to well-mapped neural circuitry, ease of controlling sensory input, and genetic accessibility. Remarkably, despite these advantages, no recordings have been made from genetically identified whisker primary afferents during active touch.

Here, we developed a preparation to simultaneously record from, and quantify mechanical input to, identified Merkel and unidentified slowly adapting (SA) and rapidly adapting (RA) afferents during active touch. We define the major mechanical sensitivities that allow our sample of Merkel and other afferents to encode the properties of actively touched objects. We reveal that Merkel and SA afferents provide a source of self-motion signals that encode whisker position within the current whisker cycle (phase). We demonstrate that this phase coding arises from a combination of external and internal stresses. Finally, we show that the distribution of preferred phases across the population of afferents, which spans the whisk cycle, reflects diversity in tuning to stresses related to whisker inertia and the activity of specific muscles.

RESULTS

Recording from Merkel and Unidentified Afferents during Whisking and Active Touch

We obtained electrophysiological recordings from Merkel afferents that innervate the whisker follicle (Ebara et al., 2002; Rice et al., 1986). An optogenetic tagging approach allowed us to
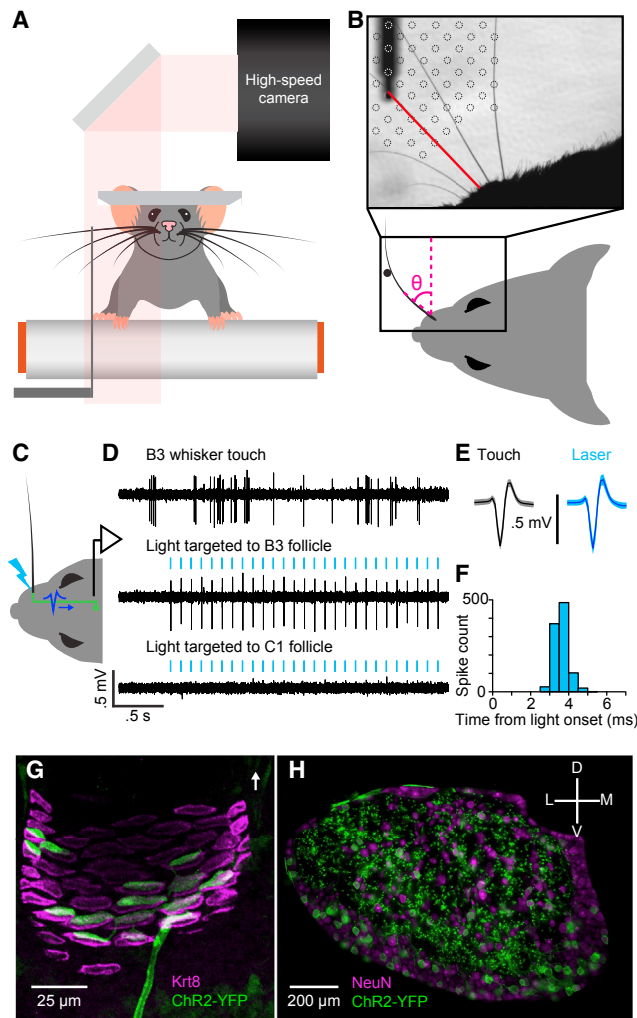
Figure 1. Recording Spikes from Merkel Afferents during Active Touch

(A) Schematic of experimental setup. A mouse whisked against a small vertical pole while head-fixed and running on a treadmill. High-speed video (500 Hz) of whiskers was obtained at the same time as electrophysiological recordings from primary afferents in the trigeminal ganglion.

(B) Image from high-speed video overlaid with example grid showing the set of pole locations used during one afferent recording. The shadow from part of the mouse face and the pole in one location (and its holder) are evident. One row of whiskers was left intact. A whisker in contact with the pole is highlighted in red. Whisker position (θ) was measured as angular displacement from the medial-lateral axis.

(C) Schematic of in vivo identification of Merkel-associated afferents by optogenetic tagging. The whisker pad was illuminated with blue light (bolt), while a recording was made from a whisker-responsive neuron in the trigeminal ganglion. Action potentials triggered by photostimulation (blue waveform) of the peripheral axon propagated to the cell body where they were recorded.

(D) Example electrophysiology traces showing spikes of a primary afferent responsive to stimulation of the B3 whisker (top) and to photostimulation targeted to the B3 whisker follicle (middle), but not to photostimulation of the nearby C1 whisker follicle (bottom). Vertical blue ticks: 2 ms light pulse.

(E) Spike waveforms (mean ± SD) in response to touch (black) and light (blue) were nearly identical (shading: SD).

(F) Histogram of latencies from light onset to time of spike (peak or trough) recorded in TG, for neuron shown in (D). Spikes occurred with short latency (mean: 3.6 ms) and low jitter (SD: 0.3 ms).

(G) Projection through a confocal z stack of a single whisker follicle (region of the ring sinus) showing a single channelrhodopsin-2 (ChR2)-expressing afferent (green), associating with Merkel cells (magenta). The Merkel cells are labeled by keratin 8 (Krt8, TROMA-I) staining. White arrow: direction of skin surface.

(H) Coronal section through the trigeminal ganglion of a $TrkC^{CreER};Rosa^{Ai32}$ mouse showing ChR2 expression (green) in both cell bodies and processes. The cell bodies are labeled by NeuN staining (magenta). See also Figure S1.
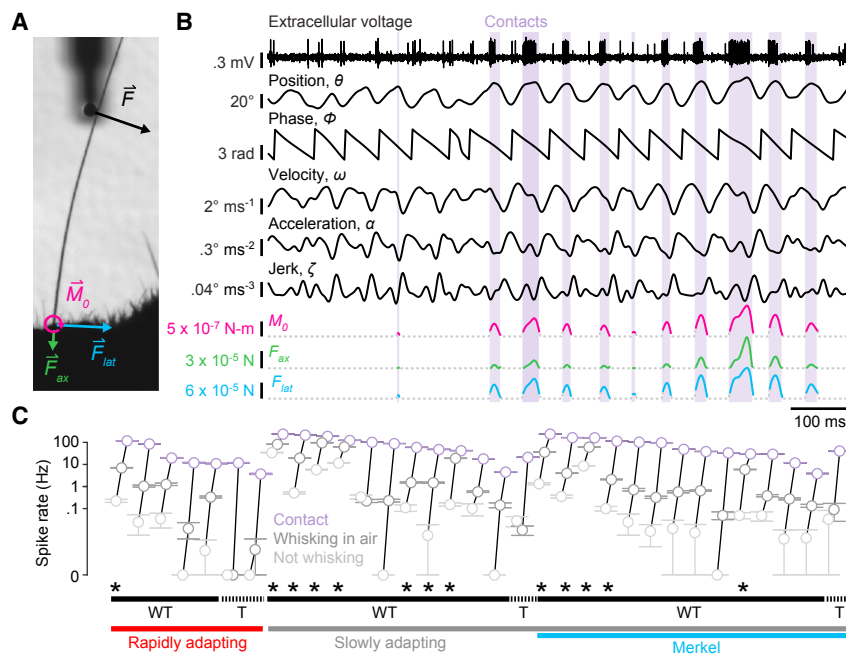
record spikes from single genetically identified Merkel afferents during behavior (Figures 1 and S1). Mice whisked freely in air and against a pole presented at multiple locations as they ran on a treadmill (Figures 1A and 1B), generating mechanical signals at the whisker base (Figure 2). We collected an initial dataset (n = 33 afferents) comprising identified Merkel afferents (n = 14), as well as unidentified SA (n = 12, likely including Merkel) and RA (n = 7) afferents.

Whisker afferents are located in the trigeminal ganglion (TG) and have receptive fields containing a single whisker (Zucker and Welker, 1969). High-speed (500 Hz) video of this whisker, combined with post hoc measurements of whisker shape and methods that model whiskers as tapered beams (Birdwell et al., 2007; Pammer et al., 2013), allowed us to estimate mechanical variables expected to cause spiking (Figure 2; Movie S1). We aligned spike times from single afferents with mechanical time series including the angular position (θ), velocity (ω), acceleration (α), and jerk (ζ, the rate of change of α) of the whisker, and the magnitudes of the two forces (F_{ax}, axial force pushing the whisker into the follicle, and F_{lat}, lateral force pushing the whisker along the face) and one bending moment (M_0, acting to bend the whisker at its base) resulting from whisker-object interactions in the plane of video imaging (Figures 2A and 2B; STAR Methods). We also quantified rates of change for the two contact forces (F'_{ax} and F'_{lat}) and bending moment (M'_0).

For our initial dataset (of 33 afferents), we obtained 54,647,500 frames of high-speed video with simultaneous single neuron recordings for analysis, corresponding to 823 min total for identified Merkel afferents, and 999 min for unidentified afferents. We assigned each video frame into one of three behavioral categories: (1) not whisking and not in contact with the pole; (2) whisking in air with no contact; and (3) whisking against the pole. To avoid ambiguous periods in which a nearly motionless whisker swayed in and out of light contact with the pole, we excluded from further analysis periods of contact without whisking.

During non-whisking periods, most Merkel and unidentified afferents spiked at low rates (Figure 2C; baseline rate 0.0 ± 0.2 Hz, median ± interquartile range (IQR), n = 33, including 14 Merkels, 12 SA, and seven RA). All afferents responded with increased spike rates during touch (whisker-pole contact; 48.0 ± 96.3 Hz, median ± IQR, n = 33). During whisking in air, most afferents responded with increased spike rates (denoted "WT" afferents to indicate both whisking and touch responsiveness, following terminology of Szwed et al., 2003; Yu et al., 2006; Figure 2C; Table S1). For a subset of WT afferents, spike rates during whisking in air were especially pronounced (Figure 2C, asterisks; 19.1 ± 58.2 Hz, median ± IQR; 13 of 33 afferents total,

Figure 2. Merkel and Unidentified Afferents Respond to Both Active Touch and Self Motion

(A) Zoomed region of a high-speed video frame showing a whisker in contact with the pole. Whisker-pole contact force $(\vec{F})$ can be decomposed into the force components acting along the axis of the whisker $(\vec{F}_{ax})$ and lateral to the face $(\vec{F}_{lat})$. The magnitudes of these forces and of the bending moment $(\vec{M}_0)$ induced by $\vec{F}$ were estimated for each video frame.

(B) Example time series for a Merkel afferent. There is 1 sec of electrophysiological recording (top trace) that is shown with mechanical variables estimated from the high-speed video, including whisker angular position (θ), phase of θ within the whisk cycle (Φ), whisker angular velocity (ω), whisker angular acceleration (α), whisker angular jerk (ζ), and magnitude of contact-induced moment (M_0), axial force (F_{ax}), and lateral force (F_{lat}). The periods of whisker-pole contact are indicated by lavender shading.

(C) Mean spike rates of neurons during periods when the mouse was not whisking (light gray symbols), during whisking in free air (dark gray), and during whisker-pole contact (lavender). The error bars indicate 95% bootstrap confidence intervals of the means. The data points for each neuron are connected by black lines. The neurons are sorted along the horizontal axis by rapidly adapting (lower red bar) or slowly adapting (lower gray bar) properties, positive Merkel afferent identification (lower blue bar), sensitivity to touch (T, upper dashed bars), or to both whisking and touch (WT, upper solid bars). A subset of afferents especially sensitive to whisking in air (referred to as WT* in the text) are indicated with asterisks. See also Movie S1.

including five Merkel, seven SA, and one RA; we denote this subset of WT afferents as WT*; STAR Methods).

Active Touch Is Encoded via Sensitivity to Moment and Its Rate of Change

To investigate coding during touch, we analyzed periods of whisker-pole contact. Merkel and SA afferents responded to contact by spiking in a slowly adapting and dramatically direction-selective manner, responding far more strongly to contacts in either the protraction or retraction direction (Figure 3A). Mice whisked freely against a pole presented at different locations, producing highly variable spike rates that reflected both whisking behavior and the tuning properties of each afferent (Figure 3B). What mechanics underlie spiking during active touch?

We fitted statistical models for each afferent to predict spike rate as a function of mechanical variables, based on single (2 ms) video frames during touch (generalized additive models, GAMs; STAR Methods). We quantified model performance using the Pearson correlation between time series of predicted and actual spike rate, after smoothing with a Gaussian kernel (σ = 4 ms). A "full" model (GAM fitted to M_0, F_{ax}, F_{lat}, M'_0, F'_{ax}, F'_{lat}, θ, ω, α, and ζ) allowed excellent recapitulation of the mean spike rate for touches at different pole locations (Figures 3B and 3C) and strongly predicted ongoing spike rate (r = 0.71 ± 0.16, mean ± SD, n = 33; Figure 3D). Comparison of statistical models revealed that individual Merkel and unidentified afferents responded to several mechanical variables (Figures S2A–S2D). Models fitted to moment or its rate of change alone explained spiking relatively poorly (r = 0.45 ± 0.19 and 0.42 ± 0.21, respectively; mean ± SD, n = 33; Figure 3D). However, M_0 and M'_0

together explained spiking (r = 0.63 ± 0.20, n = 33) better than any other pair of variables and better than a more complex model fitted to M_0, F_{ax}, and F_{lat} (r = 0.48 ± 0.19, n = 33; Figures 3D and S2C). Thus, although afferents responded to multiple mechanical variables, spiking during touch was parsimoniously accounted for by M_0 and M'_0.

To visualize the sensitivity of each afferent to M_0 and M'_0, we constructed joint tuning surfaces (Figures 3E, 3F, and S2E). These surfaces show the mean spike rate evoked by combinations of M_0 and M'_0. Individual touches corresponded to stereotypic trajectories through two of the four quadrants (Figures 3E and 3F; protraction touches: $M_0 > 0$ and retraction touches: $M_0 < 0$). Tuning surfaces revealed consistent motifs across afferents (Figures 3H, 3I, and S2E).

Moment at the base of the whisker and its rate of change were critical drivers of Merkel and SA afferent spiking during touch. Whisker bending moment causes strain in the follicle (Bagdasarian et al., 2013; Whiteley et al., 2015), which can presumably lead to Piezo channel activation and subsequent spiking. Why is rate of change of moment critical? The whisker is coupled to mechanically activated channels via viscoelastic tissues (Fraser et al., 2006; Mitchinson et al., 2004). Stress in viscoelastic materials depends on both strain and its rate of change. We therefore hypothesized that sensitivity to both M_0 and M'_0 arose from tissue viscoelasticity (cf. Fraser et al., 2006; Williams et al., 2010).

Active Touch Responses Are Predicted by a Simple Mechanical Model

We fitted a simple empirical model of viscoelastic coupling between moment at the whisker base and stress in the follicle
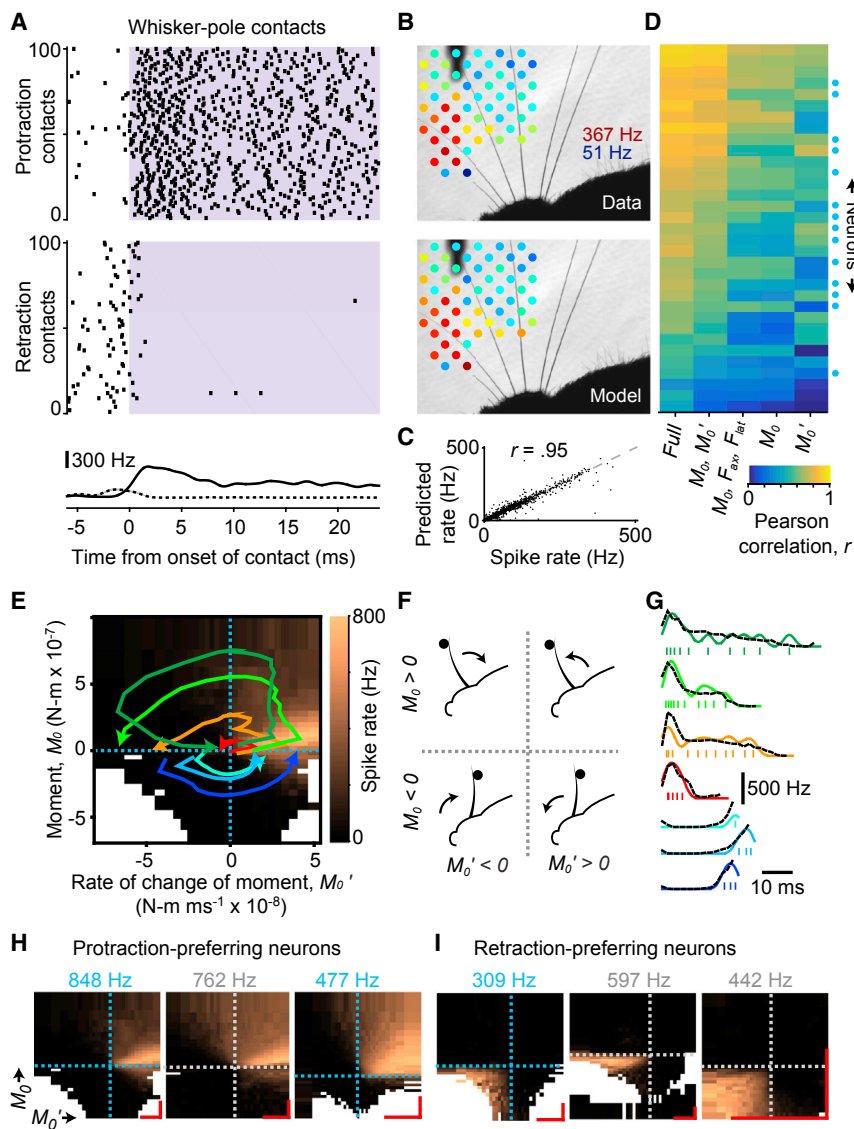
Figure 3. Active Touch Encoding via Sensitivity to Bending Moment and Its Rate of Change

(A) Example rasters showing spiking of a Merkel afferent for 100 randomly selected protraction (top raster) and retraction (bottom raster) contacts. The lavender shading indicates contact (2 ms resolution). Shown at the bottom are mean spike rates aligned to contact onset for all protraction (solid, ±SEM; n = 4,392 total) and retraction (dashed, ±SEM; n = 1,556 total) contacts. Spike rate differences prior to contact in the two rasters are due to differences in tuning to protraction and retraction self-motion.

(B) Mean spike rate (indicated by colors) during contact at each pole location (top) for an example SA afferent, and predicted spike rate from the "full" GAM statistical model (STAR Methods) fitted to predict instantaneous spikes from this neuron (bottom). The color scale for both panels is identical and ranges from 51 to 367 Hz.

(C) Actual versus predicted mean spike rates during contact, pooled across neurons and pole locations (data for each neuron as in B).

(D) Heatmap showing the Pearson correlation coefficient, r, between recorded spikes (smoothed by Gaussian kernel with σ = 4 ms) and predicted spike rates from GAM models (columns) fitted for each neuron (rows; blue circles: Merkel afferents) based on different combinations of mechanical variables.

(E) Tuning surface for example Merkel afferent (same as in A) showing mean spike rate (color scale) binned by moment (M_0) and its rate of change (M_0'). The trajectories (colored curves) for example contacts are plotted on top of the surface. Each contact begins near the origin and proceeds counter-clockwise across either the top (for protraction) or bottom (for retraction) half of the tuning surface. The dashed lines indicate axis origins. The bins with fewer than 25 observations are white.

(F) Schematic depicting the four quadrants of the M_0–M_0' tuning surface shown in (E). The whisker can be moving in the protraction or retraction direction and be in contact with a pole either in front of or behind the whisker.

(G) Spike times shown individually (ticks) and smoothed (colored curves, Gaussian kernel with

σ = 2 ms) for the example trajectories in (E), overlaid with spike rate "read off" from the tuning surface (black dashed traces).

(H) Example M_0–M_0' tuning surfaces for three neurons that preferred protraction contacts (leftmost neuron from E).

(I) Same as (H), but for three neurons that preferred retraction touches.

(H and I) Dashed lines indicate the origin of each axis and are colored by afferent type (blue: Merkel and gray: SA). The color scale for each surface ranges from 0 Hz to a maximum spike rate indicated above the surface (blue text: Merkel). The scale bars (red) indicate 2×10^{-7} N-m and 2×10^{-8} N-m ms^{-1} for M_0 and M_0', respectively. The white bins as in (E). See also Figure S2.

(Figure 4A). Our goal was to test whether such coupling could explain the responses of Merkel and SA afferents. In the model, moment was converted into strain inside the follicle according to sigmoidal functions. Strain caused elastic and viscous stresses (modeled by a spring and damper, respectively) that were then summed, rectified, and mapped linearly to spike rate up to a maximum of 1,000 Hz (Figures 4A and 4B; STAR Methods). The model postulates that the firing rate of Merkel and SA afferents is determined by instantaneous strain and its rate of change and does not depend on either stimulus or spiking history.

Remarkably, this mechanical model predicted spike rates at levels comparable to GAM statistical models (Figure 4C) and re-

produced tuning surfaces (Figure 4D). The excellent fit between data and model suggests that filtering of contact stresses by tissue viscoelasticity underlies spike rate adaptation and thus plays a central role in determining the activity of Merkel and SA afferents (Williams et al., 2010).

Merkel and Unidentified SA Afferents Encode Whisk Phase

We next investigated coding during whisking in air, in the absence of touch. The rhythmic motion of whisking can be decomposed into an amplitude, setpoint, and phase (Hill et al., 2011). The whisk phase (Φ) quantifies the position of the whisker
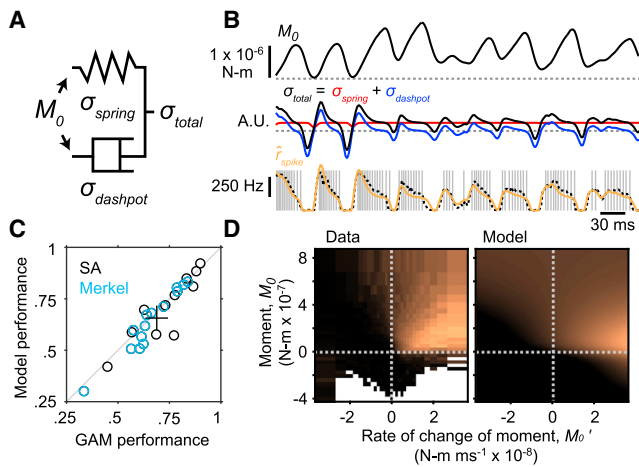
CellPress

Figure 4. A Simple Mechanical Model Predicts Responses to Active Touch

(A) Schematic of the model. Moment at the base of the whisker causes strain on a spring and dashpot arranged in parallel. The variables representing elastic (σ_{spring}) and viscous ($\sigma_{dashpot}$) stresses are summed (σ_{total}) and scaled (to a maximum of 1,000 Hz) to yield spike rate.

(B) Example model dynamics for a single touch. An example trace of moment (M_0) during a protraction contact for a recording from a Merkel afferent (dashed gray line: $M_0 = 0$) is shown (top). Elastic (red) and viscous (blue) stress variables and their sum (black; dashed gray: $\sigma = 0$) are shown (middle). Individual spike times (gray ticks) aligned to the M_0 trace are shown (bottom). The spike rate predicted from the viscoelastic model (orange) matched that predicted from the M_0–M_0' tuning surface (dashed black; left surface shown in D). This example represents a challenging trajectory containing wide ranges of M_0 and M_0'.

(C) Viscoelastic model performance was similar to that of GAM statistical models based on M_0 and M_0'. The performance of each model was quantified by the Pearson correlation coefficient, r, between model-predicted spike rates and recorded spike rates (smoothed by Gaussian kernel with $\sigma = 4$ ms). The plot symbols show individual Merkel (blue circles, n = 14) and SA (black circles, n = 11; one SA excluded because model fitting failed) afferents and the mean ± 95% bootstrap confidence interval (black lines).

(D) Tuning surfaces for real data (left) and simulated from the model (right). The color scale ranges from 0 to 500 Hz. The conventions are as in Figure 3E.

within the current protraction-retraction cycle (Curtis and Kleinfeld, 2009; Fee et al., 1997; Hill et al., 2011; Szwed et al., 2003). Here, we found that all WT* afferents were also dramatically modulated by phase, with large changes in spike rate between non-preferred and preferred phases (Figures 5A–5C; 2.1 ± 3.4 Hz versus 51.2 ± 105.7 Hz, respectively; median ± IQR; n = 15 total, including the earlier 13 WT* afferents and two additional SA afferents that were "putative" WT*: defined as responsive to manual whisker stimulation and meeting criteria for whisking in air responsiveness, but for which we did not collect whisker-pole contact data; Table S1). Preferred phase of each afferent was largely invariant across whisk cycles of different amplitudes, frequencies, and setpoints (Figure S3). Across the population of afferents, the preferred phase spanned the whisk cycle (Figures 5D and 5E).

Phase Coding Arises from External and Internal Stresses

As muscles accelerate the whisker, a net moment is produced at the base of the whisker in proportion to the acceleration, $\vec{M} = I\vec{\alpha}$,
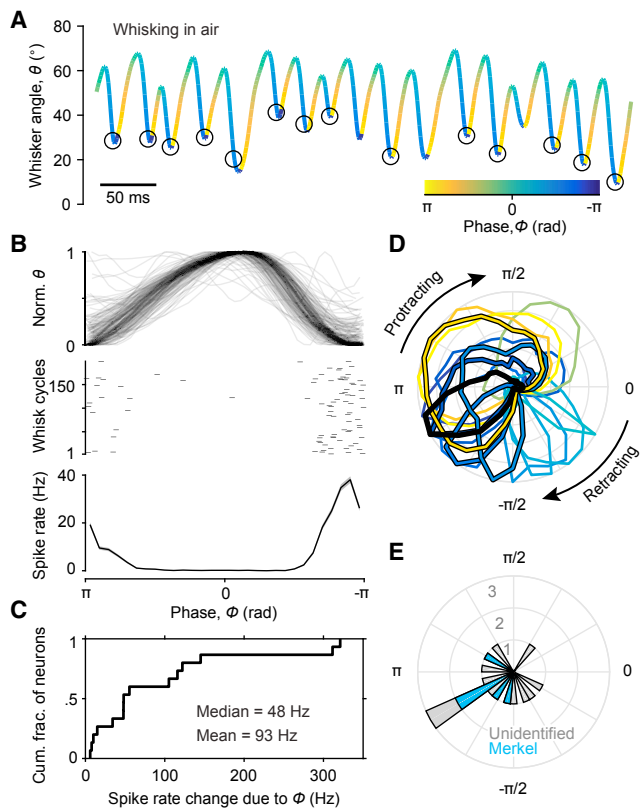

Figure 5. Self-Motion Responses Encode Whisk Phase

(A) Example whisker position trace overlaid with spike times (black circles) for a Merkel afferent during whisking in air. The color scale depicts phase within the whisk cycle. The spikes occurred near full retraction (phase of $-\pi/\pi$) during whisking.

(B) Normalized and superimposed whisker position traces (top) and spike time raster (middle) for 200 whisk cycles randomly chosen from 6,325 total cycles and mean spike rate (bottom; the "phase tuning curve"; ±SEM across all 6,325 cycles). The same afferent as in (A).

(C) Cumulative histogram showing spike rate changes due to phase modulation (maximum minus minimum of the phase tuning curve) for WT* afferents (n = 15, including 5 Merkel, 9 SA, and 1 RA).

(D) Normalized phase tuning curves for WT* afferents in polar coordinates (n = 15). The preferred phase of each afferent is indicated by colors (color scale as in A). The Merkel afferents (n = 5) include the black curve (example from A) and those with black outline.

(E) Polar histogram showing the distribution of preferred phases (peak of tuning curves from D; blue: Merkels). See also Figure S3.

where I is the moment of inertia. This moment will bend the whisker, cause strain in the follicle, and potentially open mechanically activated ion channels. However, muscle force must not only accelerate the whisker against its moment of inertia, but also overcome tissue viscoelastic forces that depend on displacement (θ) and velocity (ω) (we neglect air resistance). Mechanoreceptors may be directly sensitive to these internal (muscle and viscoelastic) forces.

To test whether phase tuning depended on $\vec{M}$, the moment caused by the whisker's resistance to rotation, we performed an experiment in which we progressively cut off distal segments of the whisker and remeasured tuning (Figure 6). In recordings
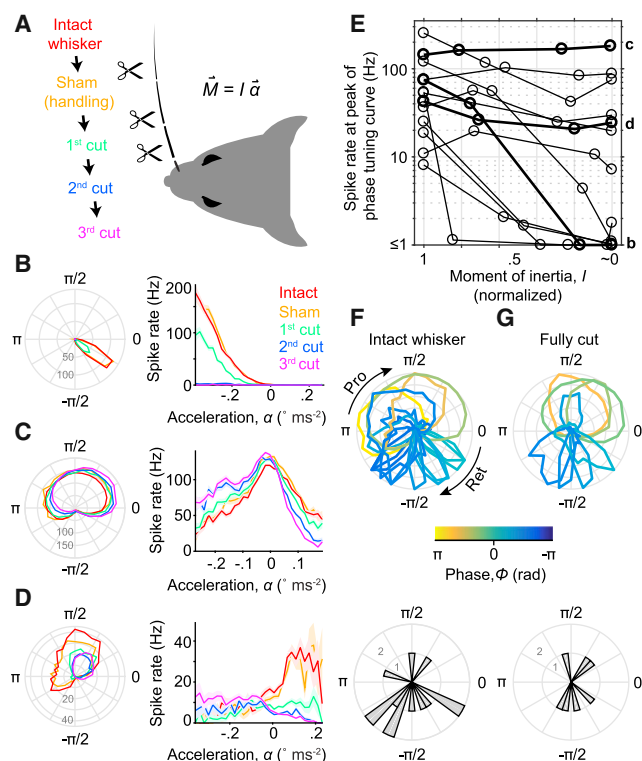
Figure 6. Self-Motion Responses Arise from Both External and Internal Stresses

(A) Schematic of the experiment. The responses during whisking in air were recorded across progressive cuts to shorten the relevant whisker and decrease its moment of inertia, I (resistance to change in angular motion). The bending moment at the base of the whisker ($\vec{M}$), proportional to I and angular acceleration ($\vec{\alpha}$), was thus progressively reduced. As a control, prior to cutting the whisker, it was handled in a sham manipulation.

(B) Tuning curves for phase (left) and acceleration (right; ±SEM) are shown for an example SA afferent across cutting conditions (colors, as in A). The afferent showed gradual reduction of spike rates down to zero as the whisker was progressively cut to its base (i.e., when $I \sim 0$). Note that preferred phase remained constant as overall spike rate decreased.

(C) Example SA afferent with little change in responses after progressive cutting even in the "fully cut" condition. The conventions are as in (B).

(D) Example SA afferent with responses that were reduced, but not eliminated, by cutting. The conventions are as in (B).

(E) Summary showing spike rate at the preferred phase for each afferent (n = 13 SA), as a function of the remaining whisker moment of inertia (normalized to intact condition). The examples from (B)–(D) are plotted with thick lines and indicated at the right by corresponding lower case letters (b, c, and d). A log scale for the spike rate axis accommodates the wide range across afferents.

(F) Overlay of normalized phase tuning curves (top) and histogram of preferred phases (bottom) for each afferent (n = 13 SA) from the intact whisker condition. The conventions are as in Figures 5D and 5E.

(G) As in (F), but for fully cut whisker conditions (n = 7; only neurons with ≥3 Hz peak response). See also Movie S2.

from a new set of putative WT* afferents (n = 13, including 12 SA and one RA), we first obtained baseline responses during whisking in air. Next, we cut off a distal portion of the whisker, thereby reducing the whisker's moment of inertia, and thus $\vec{M}$, and recorded new responses from the same afferent. We repeated this process for up to three cuts, shortening the whisker eventu-

ally to near its base (Figure 6A; final length: 0.37 ± 0.43 mm, mean ± SD, n = 13), and thus dramatically reducing its moment of inertia, $I \sim 0$, and abolishing $\vec{M}$. Spiking during whisking in air was eliminated by this manipulation for a subset (6 of 13) of afferents (Figures 6B and 6E; from 50.1 ± 42.3 Hz for intact whisker, to 0.9 ± 0.7 Hz after final cut, mean ± SD, n = 6, including five SA and one RA). Spike rates from these afferents increased with acceleration (Figure 6B; either positive or negative acceleration), as expected if whisker inertia drove spiking. Other afferents (7 of 13) showed self-motion responses that remained after cutting (Figures 6C–6E; 86.1 ± 71.5 Hz for intact whisker versus 70.3 ± 58.5 Hz after final cut, mean ± SD, n = 7 SA), with phase tuning curves that were largely (Figure 6C) or partially unchanged (Figure 6D). Thus, for some afferents, internal forces are sufficient to produce strong, phase-tuned spiking.

Strikingly, preferred phases across the population not only spanned the whisk cycle when whiskers were intact (Figures 5 and 6F), but largely did so even after whiskers were fully cut (Figure 6G). How does this distribution of phase preferences relate to the underlying mechanical sensitivities of each afferent?

Distribution of Phase Preferences Mirrors Tuning to Inertial and Muscle-Specific Stresses

Muscles controlling whisking (Dörfl, 1982; Haidarliu et al., 2010, 2015; Wineski, 1985) are active at distinct phases of the whisk cycle in rats (Hill et al., 2008). We collected simultaneous high-speed video and electromyogram (EMG) data from mice for two major muscle groups that control whisking, the intrinsic protractor (IP) and *m. nasolabialis* (NL) muscles (Figures 7A, solid curves; and S4). EMG phase modulation in mice (Figure 7A, solid curves) was similar to that in rats (Figure 7A, dashed curves; data taken from Hill et al., 2008), as expected from their isomorphic whisking musculatures (Haidarliu et al., 2010, 2015). The whisk phase was also associated with stereotyped patterns of whisker acceleration and jerk (Figures 7B and S5). Can these patterns of muscle activation and kinematics explain the phase tuning curves we observed?

We examined in further detail the phase tuning curves obtained before (Figure 7C) and after (Figure 7D) whisker trimming from individual afferents. For those afferents that continued to spike after whisker trimming, the phase tuning curves were correlated with activation of either IP or NL muscles (Figures 7D, bottom seven afferents; Pearson correlation between phase tuning and EMG curves: $r = 0.66 \pm 0.27$, mean ± SD, n = 7 SA afferents; same afferents as in 6G). Thus, spiking in these afferents after whisker trimming was likely due to muscle-induced stresses. For each afferent, we subtracted the cut-whisker phase tuning curve from the intact-whisker phase tuning curve to obtain a measure of the net spike rate "lost" at each phase following the abolishment of whisker inertia (Figure 7E). These subtracted tuning curves were correlated with positive acceleration, negative acceleration, or jerk (Figure 7E; $r = 0.71 \pm 0.19$, mean ± SD, n = 13). In separate experiments, we obtained additional recordings from putative WT* afferents (Figure 7F; n = 5 total, including three Merkel and two SA) in which the whisker had already been cut to near its base (within ~0.5 mm of the follicle). Phase tuning curves in these afferents were strongly
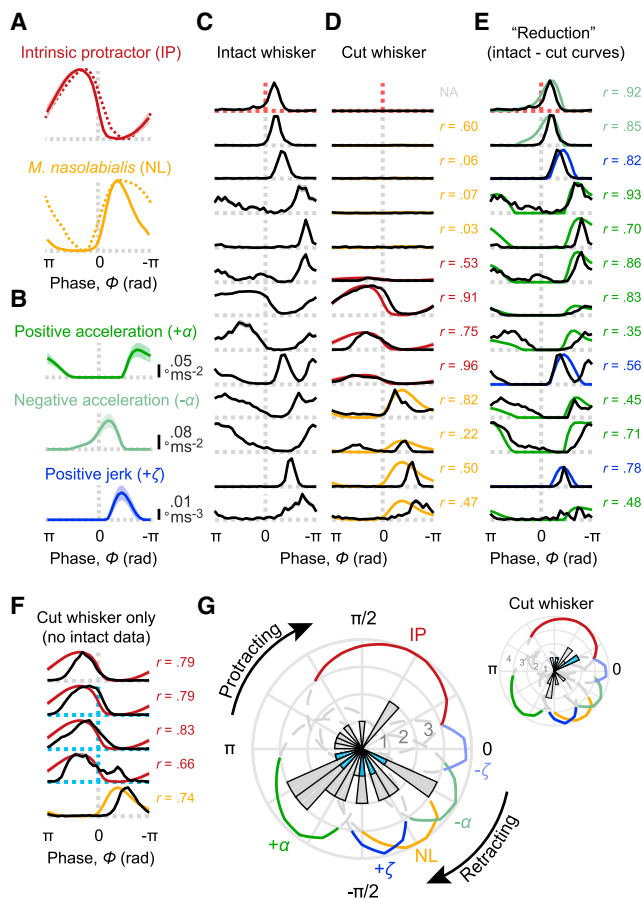
CellPress

Panel labels (Figure 7)

A
Intrinsic protractor (IP)
M. nasolabialis (NL)
π   0   -π
Phase, Φ (rad)

B
Positive acceleration (+α)   .05 |°ms^{-2}
Negative acceleration (-α)   .08 |°ms^{-2}
Positive jerk (+ζ)   .01 |°ms^{-3}
π   0   -π
Phase, Φ (rad)

C
Intact whisker
r = .60
r = .06
r = .07
r = .03
r = .53
r = .91
r = .75
r = .96
r = .82
r = .22
r = .50
r = .47
π   0   -π
Phase, Φ (rad)

D
Cut whisker
π   0   -π
Phase, Φ (rad)

E
"Reduction"
(intact - cut curves)
NA
r = .92
r = .85
r = .82
r = .93
r = .70
r = .86
r = .83
r = .35
r = .56
r = .45
r = .71
r = .78
r = .48
π   0   -π
Phase, Φ (rad)

F
Cut whisker only
(no intact data)
r = .79
r = .79
r = .83
r = .66
r = .74
π   0   -π
Phase, Φ (rad)

G
Protracting
π/2
IP
π
0
-ζ
+α
NL
+ζ
-α
Retracting
-π/2
Cut whisker
π   0

Figure 7. Phase Coding Reflects Tuning to Inertial and Muscle-Specific Stresses

(A) EMG as a function of whisk phase is shown for two main whisking muscles, the intrinsic protractors (top, solid brown; mean ± SD across n = 3 mice) and the extrinsic retractor m. nasolabialis (bottom, solid yellow; n = 1 mouse). Overlaid are published rat EMG data for the same muscles (dashed curves; obtained from Hill et al., 2008).

(B) Absolute values of positive acceleration (+α; top, dark green), negative acceleration (−α; middle, light green), and positive jerk (+ζ; bottom, dark blue) as a function of whisk phase (mean ± SD after setting values with opposite sign to 0; n = 53 recording sessions).

(C) Normalized phase tuning curves (±SEM) for afferents in the progressive whisker cutting experiment, prior to cutting (same afferents as in Figure 6E). The dashed lines indicate phase 0 (vertical dashed lines) and spike rate 0 (horizontal) and are colored by afferent type (gray: SA, n = 13 and red: RA, n = 1).

(D) Afferents from (C) shown for the fully cut whisker condition (±SEM). The afferents are aligned by rows with (C) and displayed on the same vertical scale (normalized across intact and cut conditions). The mouse EMG traces from (A) are overlaid for each afferent based on the best match (Pearson correlation coefficient between EMG and spike rate tuning curves, r, shown to right of each curve; NA: correlation not computed due to zero spikes).

(E) Same afferents as in (C) and (D), aligned by rows with same normalization, but showing apparent "reduction" in spike rate at each phase, obtained by subtracting cut from intact whisker tuning curves. The negative values were set to zero. The mean kinematics traces from (B) are overlaid for each afferent based on the best match (Pearson correlation coefficient, r, between curves; shown to right of each pair of curves; matches chosen from among ±α and ±ζ).

(F) Same as (D), but for additional afferents (n = 3 Merkel and n = 2 SA; Merkels: blue dashed lines) recorded after the whisker had already been cut.

correlated with EMG from either IP or NL muscles (Figure 7F; r = 0.76 ± 0.06, mean ± SD, n = 5).

We found striking similarities between the average phase modulation of spike rate in individual afferents and the average phase modulation on kinematic variables related to inertial forces and IP or NL muscle activity. Comparison of EMG activity with simultaneously measured whisker kinematics showed strong correlations between IP muscle activity and positive whisker velocity (Figures S4B and S4D) and between NL activity and negative velocity (Figures S4F and S4H). This suggests that statistical models fitted to instantaneous kinematic variables (which together reflect the combined actions of internal forces and whisker inertia) should be able to account for self-motion responses and their modulation by whisk phase. We again fitted GAM statistical models, this time to explain spike rate as a function of combinations of kinematic variables during periods of whisking in air for all WT* afferents (n = 28, same afferents as in Figures 5 and "intact" whisker condition of 6; Table S1). For each model, we then calculated the Pearson correlation between predicted and actual phase tuning curves (Figures S6A and S6B). While afferents typically showed poor sensitivity to single kinematic variables (position, velocity, acceleration, or jerk; θ, ω, α, or ζ), combinations of three or more variables predicted phase tuning curves nearly perfectly (full model with θ, ω, α, and ζ: r = 0.97 ± 0.04, mean ± SD, n = 28, including five Merkel, 22 SA and one RA; Figures S6A and S6B). Thus, phase tuning can also be understood as a sensitivity of each afferent to a specific region within multidimensional kinematic space (Figure S6C; our results thus confirm in identified afferents of awake mice the results of Wallach et al., 2016).

Together, our results show that phase tuning arises from external (inertial) forces and internal forces that mirror the activation of specific muscles, which in combination allow afferents to respond with preferred phases that span the whisk cycle (Figure 7G).

DISCUSSION

Our results quantify the responses of genetically identified Merkel and unidentified afferents during active touch. Merkel and SA afferents responded not only to touch, but also to self-motion. Self-motion responses encoded the position of the whisker within the current whisk cycle (whisk phase). This phase coding arose from a combination of external stresses related to the whisker's inertia and internal stresses that reflected the activity of specific whisking muscles.

Recordings from TG of anesthetized rodents have shown that spike trains from whisker afferents can encode passively applied stimuli with exquisite fidelity and temporal precision (Bale et al., 2015; Jones et al., 2004). Passive stimulation studies have

(G) Summary polar histogram showing preferred phase for all WT* afferents (n = 28, including 5 Merkels, 22 SA, and 1 RA; blue bars: Merkels). The colored traces illustrate the normalized kinematics and EMG curves from (A), (B) in polar coordinates (shown dashed and gray below 75th percentile for clarity). Histogram of preferred phase for all recordings in which the whisker was fully cut (n = 12 including 3 Merkel and 9 SA; n = 6 not plotted due to ≤3 Hz peak rate) is shown (inset). See also Figures S4–S6.

defined major features of the neural response to whisker deflection kinematics, such as deflection velocity and amplitude (Shoykhet et al., 2000; Stüttgen et al., 2008; Zucker and Welker, 1969). Studies using artificial whisking have shown that TG afferents respond to multiple features of whisker motion and touch (Szwed et al., 2003, 2006; Wallach et al., 2016).

During active touch, Merkel and SA afferents responded to multiple mechanical variables. However, responses were concisely accounted for by two variables: bending moment (M_0) and its rate of change (M_0'). Our finding that Merkel and SA afferents signal rate of change of moment (M_0') is intriguing because, together with whisker velocity (ω), this quantity can be used to compute the radial distance to a touched object and even the three-dimensional shape of complex objects (Birdwell et al., 2007; Solomon and Hartmann, 2006, 2011).

A simple mechanical model largely explained Merkel and SA afferent spiking. Modeling the whisker-follicle-afferent complex in greater detail (Lottem and Azouz, 2011; Mitchinson et al., 2004) will constitute important future work, but our bare-bones model already gives precise prediction of touch responses and insight into the function of Merkel afferents. Spike rate adaptation in our model arose from tissue viscoelasticity. Spike rate adaptation due to tissue viscoelasticity differs from other forms, such as ion channel inactivation, with different implications for sensory processing. Ion channel inactivation causes stimulus sensitivity to decrease over time and recover slowly. In viscoelastic adaptation, spikes reflect instantaneous stress at all times with no loss of sensitivity.

During whisking behavior in rodents, neurons in the brainstem (Moore et al., 2015), thalamus (Moore et al., 2015; Yu et al., 2006), and primary somatosensory cortex (Crochet and Petersen, 2006; Curtis and Kleinfeld, 2009; Fee et al., 1997; Hires et al., 2015) show responses modulated by whisk phase. In part because the whisker pad lacks classical proprioceptors such as muscle spindles (Moore et al., 2015), these self-motion responses have been hypothesized to serve a proprioceptive role, with the whisk phase providing a coordinate system for object localization (Curtis and Kleinfeld, 2009; Kleinfeld and Deschênes, 2011; Szwed et al., 2003). Primary afferent spiking at specific whisk phases has been observed during "artificial whisking" (Szwed et al., 2003; Wallach et al., 2016), in which the whiskers are moved by muscles following electrical stimulation (Zucker and Welker, 1969), and even during behavior (Campagner et al., 2016; Khatri et al., 2009; Leiser and Moxon, 2007). However, the genetic identity and mechanical sensitivities of the neurons responsible for these self-motion responses have remained elusive. Our data reveal Merkel afferents to be a likely source of these widely observed responses, with activity that (like unidentified SA afferents) was exquisitely phase tuned. Thus, Merkel afferents send proprioceptive information to the brain. The behavioral contexts that rely on whisker proprioception are under active investigation (Knutsen et al., 2006; Mehta et al., 2007; O'Connor et al., 2013).

The distribution of preferred phases across our population of afferents spanned the whisk cycle, with a slight abundance during the retraction phase (Figure 7G). Although examples of phase-tuned afferents have been shown previously (Bermejo et al., 2004; Campagner et al., 2016; Khatri et al., 2009; Leiser

and Moxon, 2007) (1–6 per paper), only two prior studies have reported samples large enough to permit analysis of the distribution of preferred phases (Szwed et al., 2003; Wallach et al., 2016). Both used artificial whisking and found, like our study in awake animals, that preferred phase spanned the whisk cycle (Szwed et al., 2003; Wallach et al., 2016). However, each study found a relative abundance of preferred phases during the protraction phase (Szwed et al., 2003; Wallach et al., 2016). Our results suggest that the preferred phase of a given afferent will depend on its sensitivity to a specific combination of external and internal stresses (Figure 7G), which could differ not only across experimental preparations, but also modes of behavior. For instance, we found individual afferents whose phase tuning mirrored that of specific muscles (intrinsic protractor and *m. nasolabialis*). The degree of activation of these muscles differs across artificial and natural whisking and may also differ across behavioral conditions. While downstream circuits receive strongly phase-tuned spiking from the population of afferents, we speculate that the shape of this distribution may vary systematically with different modes of whisking and be interpreted in the context of central signals that represent aspects of whisking other than phase (Hill et al., 2011).

Approximately a third of individual afferents responded robustly during self-motion, encoding whisk phase in the absence of touch. These afferents also responded during touch, raising the question of how self-motion responses can be "deconvolved" from touch responses. This is a problem also faced by other proprioceptive systems. Microneurography studies in humans have found, and suggested proprioceptive roles for, cutaneous afferents that respond both to touch and to voluntary movements of the hand (Edin and Abbs, 1991; Hulliger et al., 1979) and face (Johansson et al., 1988; Trulsson and Johansson, 2002). We found that a subset of Merkel and unidentified afferents respond to whisking and touch (WT), while others respond only to touch (T). Moreover, primary afferents that respond to whisking, but not touch (W) have previously been reported (Szwed et al., 2003) and may arise from Merkel- or non-Merkel afferents (Ebara et al., 2002; Rice et al., 1986) not sampled in our work. Thus, downstream circuits could deconvolve self-motion from touch responses at the population level, by comparing activity from afferents that respond to self-motion + touch with activity from those responding to either whisking or touch alone. Alternatively, self-motion and touch responses could also be separated by accelerating non-linear input-output curves in downstream circuits (Moore et al., 2015).

All Merkel and SA afferents we tested showed sensitivity to bending moment and its rate of change (Figures 3 and S2). However, they differed in other mechanical sensitivities during touch (Figures 3 and S2) and whisking in air (Figures 2C, 5, 6, and 7). Afferents overall and even identified Merkel afferents, for instance, showed different levels of responsiveness to whisking in air (Figure 2C). The whisker follicle contains several morphologically distinct mechanoreceptor types, including two populations of Merkel endings (one at the rete ridge collar, near the skin surface, the other located deeper in the region of the ring sinus; Ebara et al., 2002; Rice et al., 1986). Individual Merkel, RA (longitudinal lanceolate) (Sakurai et al., 2013) and club-like (Tonomura et al., 2015) afferents project to multiple trigeminal nuclei

CellPress

in the brainstem, and individual brainstem neurons receive convergent input from both RA and Merkel afferents (Sakurai et al., 2013). Yet these brainstem nuclei originate distinct pathways for somatosensory signals ascending to the cortex, with markedly different response properties (reviewed in: Bosman et al., 2011; Diamond et al., 2008; Feldmeyer et al., 2013; Kleinfeld and Deschênes, 2011). An intriguing speculation is that functional subtypes of Merkel afferents might project to brainstem targets in a manner more specific than the overall population. In general, a major outstanding question is how diverse afferent responses during active touch (Leiser and Moxon, 2007; Szwed et al., 2003) relate to mechanoreceptor types and their brainstem projections. Our approach, which combines quantification of sensory input during active touch with simultaneous recordings from genetically defined afferents, promises major progress on how different aspects of touch and proprioception are integrated by neural circuits.

Here, we investigated the responses of Merkel and unidentified afferents to whisking and active touch during behavior. Despite the popularity of the whisker system, only a very small number of studies have recorded from whisker afferents in behaving animals (Bush et al., 2016; Campagner et al., 2016; Khatri et al., 2009; Leiser and Moxon, 2007; Pais-Vieira et al., 2013; Yang et al., 2016). Only two of these studies measured the whisker bending necessary to estimate the forces and moments that drive spiking (Bush et al., 2016; Campagner et al., 2016). Our work supports these two studies, which both used statistical models to correlate the spiking of unidentified whisker afferents with mechanical variables estimated from high-speed video and extends them in multiple ways. First, our results are based in significant part on recordings from identified Merkel afferents (17 of 53 recordings). Second, while our results support the notion that afferent spiking is closely associated with whisker bending moment (Bush et al., 2016; Campagner et al., 2016), we show that, in addition to bending moment (M_0), its rate of change (M_0') must also be considered in order to explain spiking during touch. Third, we offer a simple mechanical model that explains these sensitivities in terms of contact forces and tissue viscoelasticity. Fourth, our data suggest that individual afferents respond to multiple mechanical variables beyond M_0 and M_0', of possible use for location coding (Pammer et al., 2013; Solomon and Hartmann, 2011). Finally, we demonstrate that phase tuning arises from both external and internal forces that reflect whisker inertia and the activity of specific muscles and suggest that, across the population of afferents, the balance of these factors allows the preferred phase to span the whisk cycle.

Together, our data suggest that Merkel afferents in the mouse whisker system are positioned to play a dual role in both proprioception and touch, sending to the brain multiplexed information in two somatosensory modalities critical for perception.

STAR★METHODS

Detailed methods are provided in the online version of this paper and include the following:

- KEY RESOURCES TABLE
- CONTACT FOR REAGENT AND RESOURCE SHARING
- EXPERIMENTAL MODEL AND SUBJECT DETAILS
  - Mice
- METHOD DETAILS
  - Surgery
  - Behavioral Training and Apparatus
  - Electrophysiology
  - Optogenetic Identification of Merkel Afferents
  - EMG Implantation Surgery
  - EMG Recording and Analysis
  - High-Speed Videography
  - Data Analysis: Tuning Curves and Tuning Surfaces
  - Data Analysis: Generalized Additive Models (GAMs)
  - Viscoelastic Model
  - Histology: Trigeminal Ganglion
  - Histology: Whisker Pad
  - Histology: Quantification
  - Whisker and Other Hair Trimming
  - Progressive Whisker Cutting Experiment
  - Video Analysis
  - Video Analysis: Pre-processing
  - Video Analysis: Identifying Tracked Whiskers
  - Video Analysis: Face Masking
  - Video Analysis: Whisker Baseline Curvature
  - Video Analysis: Whisker Bending Stiffness
  - Video Analysis: Contact Detection
  - Video Analysis: Smoothing and Differentiation
  - Video Analysis: Tracking "Surrogate" Whiskers
- QUANTIFICATION AND STATISTICAL ANALYSIS
- DATA AND SOFTWARE AVAILABILITY

REFERENCES

Abraira, V.E., and Ginty, D.D. (2013). The sensory neurons of touch. Neuron *79*, 618–639.

Bagdasarian, K., Szwed, M., Knutsen, P.M., Deutsch, D., Derdikman, D., Pietr, M., Simony, E., and Ahissar, E. (2013). Pre-neuronal morphological processing of object location by individual whiskers. Nat. Neurosci. *16*, 622–631.

Bai, L., Lehnert, B.P., Liu, J., Neubarth, N.L., Dickendesher, T.L., Nwe, P.H., Cassidy, C., Woodbury, C.J., and Ginty, D.D. (2015). Genetic identification of an expansive mechanoreceptor sensitive to skin stroking. Cell *163*, 1783–1795.

Bale, M.R., Campagner, D., Erskine, A., and Petersen, R.S. (2015). Microsecond-scale timing precision in rodent trigeminal primary afferents. J. Neurosci. *35*, 5935–5940.

Bermejo, R., Szwed, M., Friedman, W., Ahissar, E., and Zeigler, H.P. (2004). One whisker whisking: unit recording during conditioned whisking in rats. Somatosens. Mot. Res. *21*, 183–187.

Birdwell, J.A., Solomon, J.H., Thajchayapong, M., Taylor, M.A., Cheely, M., Towal, R.B., Conradt, J., and Hartmann, M.J. (2007). Biomechanical models for radial distance determination by the rat vibrissal system. J. Neurophysiol. *98*, 2439–2455.

Bosman, L.W., Houweling, A.R., Owens, C.B., Tanke, N., Shevchouk, O.T., Rahmati, N., Teunissen, W.H., Ju, C., Gong, W., Koekkoek, S.K., and De Zeeuw, C.I. (2011). Anatomical pathways involved in generating and sensing rhythmic whisker movements. Front. Integr. Nuerosci. *5*, 53.

Bush, N.E., Schroeder, C.L., Hobbs, J.A., Yang, A.E., Huet, L.A., Solla, S.A., and Hartmann, M.J. (2016). Decoupling kinematics and mechanics reveals coding properties of trigeminal ganglion neurons in the rat vibrissal system. eLife *5*, 5.

Campagner, D., Evans, M.H., Bale, M.R., Erskine, A., and Petersen, R.S. (2016). Prediction of primary somatosensory neuron activity during active tactile exploration. eLife *5*, 5.

Chang, W., Kanda, H., Ikeda, R., Ling, J., DeBerry, J.J., and Gu, J.G. (2016). Merkel disc is a serotonergic synapse in the epidermis for transmitting tactile signals in mammals. Proc. Natl. Acad. Sci. USA *113*, E5491–E5500.

Clack, N.G., O'Connor, D.H., Huber, D., Petreanu, L., Hires, A., Peron, S., Svoboda, K., and Myers, E.W. (2012). Automated tracking of whiskers in videos of head fixed rodents. PLoS Comput. Biol. *8*, e1002591.

Crawley, M.J. (2002). Statistical Computing: an Introduction to Data Analysis Using S-Plus (Wiley).

Crochet, S., and Petersen, C.C. (2006). Correlating whisker behavior with membrane potential in barrel cortex of awake mice. Nat. Neurosci. *9*, 608–610.

Curtis, J.C., and Kleinfeld, D. (2009). Phase-to-rate transformations encode touch in cortical neurons of a scanning sensorimotor system. Nat. Neurosci. *12*, 492–501.

Deschênes, M., Takatoh, J., Kurnikova, A., Moore, J.D., Demers, M., Elbaz, M., Furuta, T., Wang, F., and Kleinfeld, D. (2016). Inhibition, not excitation, drives rhythmic whisking. Neuron *90*, 374–387.

Diamond, M.E., and Arabzadeh, E. (2013). Whisker sensory system - from receptor to decision. Prog. Neurobiol. *103*, 28–40.

Diamond, M.E., von Heimendahl, M., Knutsen, P.M., Kleinfeld, D., and Ahissar, E. (2008). 'Where' and 'what' in the whisker sensorimotor system. Nat. Rev. Neurosci. *9*, 601–612.

Dörfl, J. (1982). The musculature of the mystacial vibrissae of the white mouse. J. Anat. *135*, 147–154.

Dörfl, J. (1985). The innervation of the mystacial region of the white mouse: a topographical study. J. Anat. *142*, 173–184.

Ebara, S., Kumamoto, K., Matsuura, T., Mazurkiewicz, J.E., and Rice, F.L. (2002). Similarities and differences in the innervation of mystacial vibrissal follicle-sinus complexes in the rat and cat: a confocal microscopic study. J. Comp. Neurol. *449*, 103–119.

Edin, B.B., and Abbs, J.H. (1991). Finger movement responses of cutaneous mechanoreceptors in the dorsal skin of the human hand. J. Neurophysiol. *65*, 657–670.

Fee, M.S., Mitra, P.P., and Kleinfeld, D. (1997). Central versus peripheral determinants of patterned spike activity in rat vibrissa cortex during whisking. J. Neurophysiol. *78*, 1144–1149.

Feldmeyer, D., Brecht, M., Helmchen, F., Petersen, C.C., Poulet, J.F., Staiger, J.F., Luhmann, H.J., and Schwarz, C. (2013). Barrel cortex function. Prog. Neurobiol. *103*, 3–27.

Fraser, G., Hartings, J.A., and Simons, D.J. (2006). Adaptation of trigeminal ganglion cells to periodic whisker deflections. Somatosens. Mot. Res. *23*, 111–118.

Haidarliu, S., Simony, E., Golomb, D., and Ahissar, E. (2010). Muscle architecture in the mystacial pad of the rat. Anat. Rec. (Hoboken) *293*, 1192–1206.

Haidarliu, S., Kleinfeld, D., Deschênes, M., and Ahissar, E. (2015). The musculature that drives active touch by vibrissae and nose in mice. Anat. Rec. (Hoboken) *298*, 1347–1358.

Hastie, T., Tibshirani, R., and Friedman, J.H. (2009). The Elements of Statistical Learning: Data Mining, Inference, and Prediction, Second Edition (Springer).

Hill, D.N., Bermejo, R., Zeigler, H.P., and Kleinfeld, D. (2008). Biomechanics of the vibrissa motor plant in rat: rhythmic whisking consists of triphasic neuromuscular activity. J. Neurosci. *28*, 3438–3455.

Hill, D.N., Curtis, J.C., Moore, J.D., and Kleinfeld, D. (2011). Primary motor cortex reports efferent control of vibrissa motion on multiple timescales. Neuron *72*, 344–356.

Hires, S.A., Gutnisky, D.A., Yu, J., O'Connor, D.H., and Svoboda, K. (2015). Low-noise encoding of active touch by layer 4 in the somatosensory cortex. eLife *4*, 4.

Hires, S.A., Schuyler, A., Sy, J., Huang, V., Wyche, I., Wang, X., and Golomb, D. (2016). Beyond cones: an improved model of whisker bending based on measured mechanics and tapering. J. Neurophysiol. *116*, 812–824.

Hulliger, M., Nordh, E., Thelin, A.E., and Vallbo, A.B. (1979). The responses of afferent fibres from the glabrous skin of the hand during voluntary finger movements in man. J. Physiol. *291*, 233–249.

Iggo, A., and Muir, A.R. (1969). The structure and function of a slowly adapting touch corpuscle in hairy skin. J. Physiol. *200*, 763–796.

Ikeda, R., Cha, M., Ling, J., Jia, Z., Coyle, D., and Gu, J.G. (2014). Merkel cells transduce and encode tactile stimuli to drive Aβ-afferent impulses. Cell *157*, 664–675.

Johansson, R.S., Trulsson, M., Olsson, K.A., and Abbs, J.H. (1988). Mechanoreceptive afferent activity in the infraorbital nerve in man during speech and chewing movements. Exp. Brain Res. *72*, 209–214.

Johnson, K.O. (2001). The roles and functions of cutaneous mechanoreceptors. Curr. Opin. Neurobiol. *11*, 455–461.

Johnson, K.O., and Hsiao, S.S. (1992). Neural mechanisms of tactual form and texture perception. Annu. Rev. Neurosci. *15*, 227–250.

Johnson, K.O., Yoshioka, T., and Vega-Bermudez, F. (2000). Tactile functions of mechanoreceptive afferents innervating the hand. J. Clin. Neurophysiol. *17*, 539–558.

Jones, L.M., Depireux, D.A., Simons, D.J., and Keller, A. (2004). Robust temporal coding in the trigeminal system. Science *304*, 1986–1989.

Khatri, V., Bermejo, R., Brumberg, J.C., Keller, A., and Zeigler, H.P. (2009). Whisking in air: encoding of kinematics by trigeminal ganglion neurons in awake rats. J. Neurophysiol. *101*, 1836–1846.

Kleinfeld, D., and Deschênes, M. (2011). Neuronal basis for object location in the vibrissa scanning sensorimotor system. Neuron *72*, 455–468.

Knutsen, P.M., Pietr, M., and Ahissar, E. (2006). Haptic object localization in the vibrissal system: behavior and performance. J. Neurosci. *26*, 8451–8464.

Knutsen, P.M., Biess, A., and Ahissar, E. (2008). Vibrissal kinematics in 3D: tight coupling of azimuth, elevation, and torsion across different whisking modes. Neuron *59*, 35–42.

Leiser, S.C., and Moxon, K.A. (2007). Responses of trigeminal ganglion neurons during natural whisking behaviors in the awake rat. Neuron *53*, 117–133.

Lottem, E., and Azouz, R. (2011). A unifying framework underlying mechanotransduction in the somatosensory system. J. Neurosci. *31*, 8520–8532.

Madisen, L., Zwingman, T.A., Sunkin, S.M., Oh, S.W., Zariwala, H.A., Gu, H., Ng, L.L., Palmiter, R.D., Hawrylycz, M.J., Jones, A.R., et al. (2010). A robust and high-throughput Cre reporting and characterization system for the whole mouse brain. Nat. Neurosci. *13*, 133–140.

Madisen, L., Mao, T., Koch, H., Zhuo, J.M., Berenyi, A., Fujisawa, S., Hsu, Y.W., Garcia, A.J., 3rd, Gu, X., Zanella, S., et al. (2012). A toolbox of Cre-dependent optogenetic transgenic mice for light-induced activation and silencing. Nat. Neurosci. *15*, 793–802.

Maksimovic, S., Nakatani, M., Baba, Y., Nelson, A.M., Marshall, K.L., Wellnitz, S.A., Firozi, P., Woo, S.H., Ranade, S., Patapoutian, A., and Lumpkin, E.A. (2014). Epidermal Merkel cells are mechanosensory cells that tune mammalian touch receptors. Nature *509*, 617–621.

Maravall, M., and Diamond, M.E. (2014). Algorithms of whisker-mediated touch perception. Curr. Opin. Neurobiol. *25*, 176–186.

Mehta, S.B., Whitmer, D., Figueroa, R., Williams, B.A., and Kleinfeld, D. (2007). Active spatial perception in the vibrissa scanning sensorimotor system. PLoS Biol. *5*, e15.

Mitchinson, B., Gurney, K.N., Redgrave, P., Melhuish, C., Pipe, A.G., Pearson, M., Gilhespy, I., and Prescott, T.J. (2004). Empirically inspired simulated electro-mechanical model of the rat mystacial follicle-sinus complex. Proc. Biol. Sci. *271*, 2509–2516.

Moore, J.D., Mercer Lindsay, N., Deschênes, M., and Kleinfeld, D. (2015). Vibrissa self-motion and touch are reliably encoded along the same somatosensory pathway from brainstem through thalamus. PLoS Biol. *13*, e1002253.

O'Connor, D.H., Clack, N.G., Huber, D., Komiyama, T., Myers, E.W., and Svoboda, K. (2010). Vibrissa-based object localization in head-fixed mice. J. Neurosci. *30*, 1947–1967.

O'Connor, D.H., Hires, S.A., Guo, Z.V., Li, N., Yu, J., Sun, Q.Q., Huber, D., and Svoboda, K. (2013). Neural coding during active somatosensation revealed using illusory touch. Nat. Neurosci. *16*, 958–965.

Pais-Vieira, M., Lebedev, M.A., Wiest, M.C., and Nicolelis, M.A. (2013). Simultaneous top-down modulation of the primary somatosensory cortex and thalamic nuclei during active tactile discrimination. J. Neurosci. *33*, 4076–4093.

Pammer, L., O'Connor, D.H., Hires, S.A., Clack, N.G., Huber, D., Myers, E.W., and Svoboda, K. (2013). The mechanical variables underlying object localization along the axis of the whisker. J. Neurosci. *33*, 6726–6741.

Preibisch, S., Saalfeld, S., and Tomancak, P. (2009). Globally optimal stitching of tiled 3D microscopic image acquisitions. Bioinformatics *25*, 1463–1465.

Quist, B.W., Faruqi, R.A., and Hartmann, M.J. (2011). Variation in Young's modulus along the length of a rat vibrissa. J. Biomech. *44*, 2775–2781.

Ranade, S.S., Woo, S.H., Dubin, A.E., Moshourab, R.A., Wetzel, C., Petrus, M., Mathur, J., Bégay, V., Coste, B., Mainquist, J., et al. (2014). Piezo2 is the major transducer of mechanical forces for touch sensation in mice. Nature *516*, 121–125.

Rice, F.L., Mance, A., and Munger, B.L. (1986). A comparative light microscopic analysis of the sensory innervation of the mystacial pad. I. Innervation of vibrissal follicle-sinus complexes. J. Comp. Neurol. *252*, 154–174.

Sakurai, K., Akiyama, M., Cai, B., Scott, A., Han, B.X., Takatoh, J., Sigrist, M., Arber, S., and Wang, F. (2013). The organization of submodality-specific touch afferent inputs in the vibrissa column. Cell Rep. *5*, 87–98.

Shoykhet, M., Doherty, D., and Simons, D.J. (2000). Coding of deflection velocity and amplitude by whisker primary afferent neurons: implications for higher level processing. Somatosens. Mot. Res. *17*, 171–180.

Solomon, J.H., and Hartmann, M.J. (2006). Biomechanics: robotic whiskers used to sense features. Nature *443*, 525.

Solomon, J.H., and Hartmann, M.J. (2011). Radial distance determination in the rat vibrissal system and the effects of Weber's law. Philos. Trans. R. Soc. Lond. B Biol. Sci. *366*, 3049–3057.

Stüttgen, M.C., Kullmann, S., and Schwarz, C. (2008). Responses of rat trigeminal ganglion neurons to longitudinal whisker stimulation. J. Neurophysiol. *100*, 1879–1884.

Suter, B.A., O'Connor, T., Iyer, V., Petreanu, L.T., Hooks, B.M., Kiritani, T., Svoboda, K., and Shepherd, G.M. (2010). Ephus: multipurpose data acquisition software for neuroscience experiments. Front. Neural Circuits *4*, 100.

Szwed, M., Bagdasarian, K., and Ahissar, E. (2003). Encoding of vibrissal active touch. Neuron *40*, 621–630.

Szwed, M., Bagdasarian, K., Blumenfeld, B., Barak, O., Derdikman, D., and Ahissar, E. (2006). Responses of trigeminal ganglion neurons to the radial distance of contact during active vibrissal touch. J. Neurophysiol. *95*, 791–802.

Taniguchi, H., He, M., Wu, P., Kim, S., Paik, R., Sugino, K., Kvitsiani, D., Fu, Y., Lu, J., Lin, Y., et al. (2011). A resource of Cre driver lines for genetic targeting of GABAergic neurons in cerebral cortex. Neuron *71*, 995–1013.

Taylor, J.R. (1997). An Introduction to Error Analysis: the Study of Uncertainties in Physical Measurements, Second Edition (University Science Books).

Tonomura, S., Ebara, S., Bagdasarian, K., Uta, D., Ahissar, E., Meir, I., Lampl, I., Kuroda, D., Furuta, T., Furue, H., and Kumamoto, K. (2015). Structure-function correlations of rat trigeminal primary neurons: Emphasis on club-like endings, a vibrissal mechanoreceptor. Proc. Jpn. Acad., Ser. B, Phys. Biol. Sci. *91*, 560–576.

Trulsson, M., and Johansson, R.S. (2002). Orofacial mechanoreceptors in humans: encoding characteristics and responses during natural orofacial behaviors. Behav. Brain Res. *135*, 27–33.

Wallach, A., Bagdasarian, K., and Ahissar, E. (2016). On-going computation of whisking phase by mechanoreceptors. Nat. Neurosci. *19*, 487–493.

Whiteley, S.J., Knutsen, P.M., Matthews, D.W., and Kleinfeld, D. (2015). Deflection of a vibrissa leads to a gradient of strain across mechanoreceptors in a mystacial follicle. J. Neurophysiol. *114*, 138–145.

Williams, A.L., Gerling, G.J., Wellnitz, S.A., Bourdon, S.M., and Lumpkin, E.A. (2010). Skin relaxation predicts neural firing rate adaptation in SAI touch receptors. Conference proceedings: Annual International Conference of the IEEE Engineering in Medicine and Biology Society IEEE Engineering in Medicine and Biology Society Annual Conference 2010, 6678–6681.

Wineski, L.E. (1985). Facial morphology and vibrissal movement in the golden hamster. J. Morphol. *183*, 199–217.

Woo, S.H., Ranade, S., Weyer, A.D., Dubin, A.E., Baba, Y., Qiu, Z., Petrus, M., Miyamoto, T., Reddy, K., Lumpkin, E.A., et al. (2014). Piezo2 is required for Merkel-cell mechanotransduction. Nature *509*, 622–626.

Wood, S.N. (2006). Generalized Additive Models: an Introduction with R (Chapman & Hall/CRC).

Woodbury, C.J., and Koerber, H.R. (2007). Central and peripheral anatomy of slowly adapting type I low-threshold mechanoreceptors innervating trunk skin of neonatal mice. J. Comp. Neurol. *505*, 547–561.

Yang, H., Kwon, S.E., Severson, K.S., and O'Connor, D.H. (2016). Origins of choice-related activity in mouse somatosensory cortex. Nat. Neurosci. *19*, 127–134.

Yu, C., Derdikman, D., Haidarliu, S., and Ahissar, E. (2006). Parallel thalamic pathways for whisking and touch signals in the rat. PLoS Biol. *4*, e124.

Zucker, E., and Welker, W.I. (1969). Coding of somatic sensory input by vibrissae neurons in the rat's trigeminal ganglion. Brain Res. *12*, 138–156.

CellPress

STAR★METHODS

KEY RESOURCES TABLE

REAGENT or RESOURCE	SOURCE	IDENTIFIER
Antibodies		
Rabbit monoclonal anti-NeuN	Millipore	Cat #: MABN140; RRID: AB_2571567
Goat polyclonal anti-Rabbit, Alexa 647	Thermo Fisher Scientific	Cat #: A-21244; RRID: AB_2535812
Rat monoclonal anti-Cytokeratin 8/18	DSHB, University of Iowa	Cat #: TROMA-I; RRID: AB_531826
Goat polyclonal anti-Rat, Alexa 647	Thermo Fisher Scientific	Cat #: A-21247; RRID: AB_141778
Rabbit polyclonal anti-GFP	Millipore	Cat #: AB3080P; RRID: AB_2630379
Rabbit polyclonal anti-RFP	Rockland	Cat #: 600-401-379S; RRID: AB_11182807
Goat polyclonal anti-Rabbit, Alexa 488	Thermo Fisher Scientific	Cat #: A-11008; RRID: AB_143165
Chemicals, Peptides, and Recombinant Proteins		
Tamoxifen	Toronto Research Chemicals	Cat #: T006000
Experimental Models: Organisms/Strains		
Mouse: TrkC^{CreER}	Bai et al., 2015	N/A
Mouse: Cck$^{tm1.1(cre)Zjh}$	The Jackson Laboratory	JAX: 019021
Mouse: B6;129S-Gt(ROSA)26Sor$^{tm32(CAG-COP4*H134R/EYFP)Hze}$/J	The Jackson Laboratory	JAX: 012569
Mouse: B6.Cg-Gt(ROSA)26Sor$^{tm9(CAG-tdTomato)Hze}$/J	The Jackson Laboratory	JAX: 007909
Mouse: CD-1 (IGS)	Charles River Labs	CR: 022
Software and Algorithms		
MATLAB v.2014a and v.2016b	MathWorks	RRID: SCR_001622
R v.3.3.2	The R Foundation for Statistical Computing	https://www.r-project.org/
mgcv package for R, v.1.8-16	Wood, 2006	https://www.CRAN.R-project.org/package=mgcv
Ephus	Suter et al., 2010; Vidrio Technologies	http://www.scanimage.vidriotechnologies.com/display/ephus/Ephus
StreamPix 5	Norpix	https://www.norpix.com/products/streampix/streampix.php
WaveSurfer	HHMI Janelia Research Campus	http://www.wavesurfer.janelia.org
MClust, v.4.1 and v.4.4	A.D. Redish	http://www.redishlab.neuroscience.umn.edu/MClust/MClust.html
Janelia Whisker Tracker	Clack et al., 2012	https://www.janelia.org/open-science/whisk-whisker-tracking
Other		
High speed CMOS camera	PhotonFocus	DR1-D1312-200-G2-8
Telecentric lens	Edmund Optics	Cat #: 55-349
Laser, 473 nm	UltraLasers	DHOM-M-473-200
Tungsten microelectrode	WPI	Cat #: TM33A20
Tungsten microwire	A-M Systems	Cat #: 795500
Suture thread	Fine Science Tools	Cat #: 12051-08

CONTACT FOR REAGENT AND RESOURCE SHARING

Further information and requests for resources and reagents should be directed to and will be fulfilled by the Lead Contact, Daniel H. O'Connor (dan.oconnor@jhmi.edu).

CellPress

EXPERIMENTAL MODEL AND SUBJECT DETAILS

All procedures were in accordance with protocols approved by the Johns Hopkins University Animal Care and Use Committee.

Mice

$Rosa^{Ai32/Ai32}$ (Jackson Labs: 012569; $B6;129S\text{-}Gt(ROSA)26Sor^{tm32(CAG\text{-}COP4*H134R/EYFP)Hze}/J$) mice (Madisen et al., 2012) on a mixed background were mated with $TrkC^{CreER/+}$ mice (Bai et al., 2015). Date of conception was marked by observation of vaginal plug. To induce CreER–based recombination at embryonic dates E11.5-E13.5, pregnant females were dosed by oral gavage with 1.5 mg tamoxifen (Toronto Research Chemicals) dissolved in sunflower oil (Sigma). Pups were delivered by Caesarian section at E19-E19.5 and reared by a CD1 foster mother (Charles River). For histological quantification of afferent labeling, $TrkC^{CreER/+}$ mice were crossed with $Rosa^{Ai9/Ai9}$ (Jackson Labs: 007909; $B6.Cg\text{-}Gt(ROSA)26Sor^{tm9(CAG\text{-}tdTomato)Hze}/J$) mice (Madisen et al., 2010) instead of $Rosa^{Ai32/Ai32}$ mice but otherwise generated identically. $Cck^{Cre/Cre}$ (Jackson Labs: 019021; $Cck^{tm1.1(cre)Zjh}$) mice (Taniguchi et al., 2011) were crossed with $Rosa^{Ai32/Ai32}$ mice. During behavior and recording experiments, mice were housed singly in a vivarium with reverse light-dark cycle (12 hr each phase). Behavior experiments were conducted during the dark (active) cycle. The sex and line of each mouse used for recordings is detailed in Table S1.

METHOD DETAILS

Surgery

Adult mice (6-18 weeks old) were implanted with titanium headposts (Yang et al., 2016). Prior to electrophysiological recordings, two small openings (0.5 mm anterior-posterior, 2 mm medial-lateral) in the skull were made centered at 0.0 and 1.0 mm anterior and 1.5 mm lateral to Bregma. Dura were left intact. Craniotomies were covered acutely with gelatin sponge (VetSpon) or chronically with silicone elastomer (Kwik-Cast, WPI) under a layer of dental acrylic (Jet Repair Acrylic).

Behavioral Training and Apparatus

Mice received 1 mL/day of water for $\geq$ 7 days prior to training. Mice were head-fixed and placed on a custom linear treadmill in order to promote whisking, because mice whisk as they run. Running was encouraged by providing water reward following voluntary bouts of running. Water was delivered via a custom "lickport" under control of Bcontrol software (C. Brody, Princeton University). On training days (2-10 days total), mice were weighed before and after each training session to determine water consumed. If mice consumed < 1 mL, additional water was given to achieve 1 mL total.

A 0.500 mm diameter class ZZ gage pin (Vermont Gage) was oriented vertically and placed in range of the whiskers. The top of the pole was elevated above the remaining whiskers but remained within the depth of high-speed video focus. The X-Y position of the pole was controlled via two stepper motors and translation stages (O'Connor et al., 2010).

Electrophysiology

The awake mouse was head-fixed and allowed to run on the linear treadmill. The craniotomy was exposed and covered with PBS. A single tungsten recording electrode (2 MΩ nominal, Parylene coated; WPI) was lowered ~5.5 mm until it reached the trigeminal ganglion. Activity was monitored by audio monitor (A-M Systems). The tissue was allowed to relax at least 10 min to stabilize recordings. An identical reference electrode was lowered to a similar depth. The differential electrophysiological signal between recording and reference electrodes was amplified 10,000x, bandpass filtered between 300 Hz and 3,000 Hz (DAM80, WPI) and acquired at 20 kHz using Ephus (Suter et al., 2010) or WaveSurfer (http://www.wavesurfer.janelia.org). Data were acquired in 5 s "trials" synchronized with high-speed video. A micromanipulator (Sutter Instruments) advanced the recording electrode until a well-isolated unit responsive to manual whisker stimulation was encountered. The unit's receptive field, response type (RA or SA), and direction selectivity were manually classified. All whiskers except the row containing the whisker-of-interest (WOI) were trimmed short with microdissection scissors. The pole was moved to regular locations spaced within range of the WOI. The mouse was coaxed to run by small manual movements of the treadmill belt. While running, mice whisked against the stationary pole. Immediately subsequent to recording, under light isoflurane the WOI was plucked with forceps for post hoc measurements of whisker geometry. After recording sessions, the craniotomy was covered with silicone elastomer and a thin layer of dental acrylic. Spike waveforms were obtained by thresholding high-pass filtered (500 Hz) traces and clustered using MClust-4.1 or MClust-4.4 (AD Redish et al.).

Optogenetic Identification of Merkel Afferents

Our tamoxifen dosing conditions in $TrkC^{CreER/+}$ mice result in labeling of SA1-Merkel afferents and proprioceptors (Bai et al., 2015). We used an intersectional strategy in which we capitalized on the lack of spindle-type proprioceptors in the whisker pad (Moore et al., 2015), and the single whisker receptive fields of TG neurons (Zucker and Welker, 1969), in order to avoid recording from proprioceptors. Specifically, afferents that were both light responsive and had clear responses to manual stimulation of a single whisker were considered to be "Merkel" afferents. Neurons were tested for light sensitivity by manually directing laser illumination (473 nm; UltraLasers, DHOM-M-473-200) to a whisker pad location centered on the follicle corresponding to the neuron's whisker receptive field (~100 mW out of a 200 μm, 0.39 NA fiber; fiber was hand-held but positioned ~2-3 mm from the skin). Light pulses were

triggered and acquired simultaneously with electrophysiology traces by Ephus. High-speed video was simultaneously recorded and inspected post hoc to eliminate the possibility of movement-related activity. Spikes from optogenetic stimulation trials were clustered together with spikes from all other (non-stimulation) trials. Because TG neurons are not known to synaptically excite one another, "indirect" excitation can occur only through a loop involving sensory-motor loops and mechanical excitation. Thus, with powerful light excitation in a subset of $TrkC^{CreER};Rosa^{Ai32}$ mice we observed a light-evoked whisker movement ("twitch") visible on high-speed video at latencies as short as ~25 ms. However, we accepted only neurons that spiked at short latency (< 8 ms; 4.9 ± 1.3 ms; mean ± SD) and with low jitter (SD of first-spike latency: 0.91 ± 0.29 ms; Figures S1C and S1D) following onset of a brief light pulses (< 10 ms; typically 2-4 ms) delivered infrequently (0.4-10 Hz). Many but not all accepted neurons followed 10 Hz trains (not shown); however, our hand-held optical fiber did not permit quantitative analysis of spike reliability. Inspection of high-speed video showed that our light-identified neurons responded even when no twitch was evoked (not shown). In searching for light-responsive neurons, we directed the light not only to the follicle of interest, but also to distant parts of the whisker pad (> 1 whisker away; expected to evoke the same twitches) and confirmed specificity (Figure 1). We found that we could evoke spiking (not shown) by directing light to a region caudal to the whisker pad, where afferent fibers come together into the infraorbital nerve (Dörfl, 1985), indicating that afferents could be excited by illumination of their processes outside the follicle. We did not rely on stimulation of this caudal location while searching for light-activated units, because it evoked strong whisker twitches due, presumably, to synchronous excitation of many afferents.

An alternative approach to exciting Merkel cell-associated primary afferents is to excite the afferents synaptically via ChR2 excitation of Merkel cells themselves (Maksimovic et al., 2014). The Cck^{Cre} line labels Merkel cells (Maksimovic et al., 2014), but also other tissue in the whisker pad including muscle cells. We could trigger clear muscle contractions at multiple locations on the body by local light stimulation in $Cck^{Cre};Rosa^{Ai32}$ mice (not shown). Thus, in practice we found it difficult to obtain spikes with sufficiently short latencies as to be unambiguously evoked by light stimulation per se rather than mechanically via ChR2-based muscle excitation. We therefore focused on the $TrkC^{CreER};Rosa^{Ai32}$ mice, but did include one light-identified neuron from a $Cck^{Cre};Rosa^{Ai32}$ mouse that met our criteria (7.9 ± 1.3 ms latency to spike; mean ± SD).

EMG Implantation Surgery

Adult mice (6-26 weeks old) were implanted with titanium headposts (Yang et al., 2016) and allowed at least 2 days to recover. Electrodes were made by connecting PFA coated tungsten microwire (50 μm, A-M Systems, #795500) to gold-plated pins (WPI, #5482). The pins were insulated with heat-shrink tubing, and then glued together and fixed to the headpost using cyanoacrylate glue (Krazy Glue) and dental acrylic (Jet Repair Acrylic). An incision was made in the skin caudal or dorsal to the target muscle. One pair of wires was implanted in each mouse into either *m. nasolabialis* or the intrinsic protractors. The coating at the end of each wire was stripped 0.5-1.0 mm and bent to form a hook. The hooked end of each wire was placed into the beveled end of a 30G needle (BD, #305128) to shuttle it beneath the skin to the target muscle. The two wires were placed ~1 mm from each other in the target muscle. Bipolar current was applied across the pair of wires using a stimulus isolator (WPI, A365) to induce movement. Implantation was considered successful if minimal stimulation (25-100 μA) produced movement characteristic of the target muscle (*m. nasolabialis*, pad retraction; intrinsic protractors, specific protraction of a few adjacent whiskers). The incision was sutured closed (8/0, Fine Science Tools #12051-08) and covered with antibiotic ointment (Pac-Kit). Mice were allowed at least 1 day to recover before recording.

EMG Recording and Analysis

Fur and all whiskers except those in C row were trimmed short with microdissection scissors (Fine Science Tools). The mouse was head-fixed and allowed to run on the treadmill. EMG signals were acquired in 5 s trials synchronized with high-speed whisker video. The differential signal between the two wires was amplified 1,000x, bandpass filtered between 1 Hz and 10 kHz (DAM80, WPI) and acquired at 20 kHz using Ephus. After recording, signals were bandpass filtered between 400 Hz and 3 kHz (Butterworth, 7th order). For intrinsic protractor recordings, the signal was then rectified and binned to obtain the mean rectified EMG for each 2 ms high-speed video frame. For the *m. nasolabialis* recording, we observed apparent motor unit spikes (Deschênes et al., 2016), and obtained the times of these spikes by thresholding the bandpass filtered signal. The *m. nasolabialis* phase tuning curve (Figures 7A, S4G, and S4H) was then obtained using these motor unit spike times. Whisk phase was determined by tracking a C-row or Greek whisker.

High-Speed Videography

Video frames (640 pixels x 480 pixels, 32 μm/pixel) were acquired at 500 Hz using a PhotonFocus DR1-D1312-200-G2-8 camera (90 μs exposure time) and Streampix 5 software (Norpix). Light from a 940 nm LED (Roithner Laser) was passed through a condenser lens (Thorlabs) and directed into a 0.25X telecentric lens (Edmund Optics) after passing through the whisker field. Ephus triggered individual camera frames (5 s, 2,500 frames per trial) synchronized with electrophysiological recordings.

Data Analysis: Tuning Curves and Tuning Surfaces

Tuning curves and surfaces were constructed after removing outliers (defined in "Glossary" subsection below). Phase tuning curves were formed by binning data into 30 bins with approximately equal numbers of observations in each. For tuning surfaces, the range of each variable of interest was divided into 10 (for θ_{amp}, $\theta_{setpoint}$ and f_{whisk}) or 30 (all other variables) equally spaced bins, unless otherwise noted. Bins with < 25 observations were removed from analysis and appear white in the surfaces. The color scale for surfaces

depicts the mean spike rate (for single unit recordings, in Hz) or voltage (for intrinsic protractor EMG, in mV) for each bin, and is scaled linearly from 0 to the maximum for each surface. For M_0 versus M_0' tuning surfaces, in order to more uniformly distribute observations among bins, we used non-uniform bin sizes as follows. First, observations were transformed by the sigmoidal function:

$$y = \frac{2}{1 + e^{-k*x}} - 1,$$

where x was the raw observation value, y was the transformed value, and k was a factor controlling the degree of non-linearity. For M_0, F_{ax}, and F_{lat}, k was the inverse of the 80th percentile value for the distribution of each variable. For M_0', F_{ax}', and F_{lat}', k was the inverse of the 90th percentile value. Bins were determined as described above, and then data were transformed back using the inverse function:

$$x = -\frac{1}{k}[\log(1 - y) - \log(1 + y)].$$

We note that our tuning surfaces show responses only to combinations of mechanical variables obtained through whisking, rather than to arbitrary combinations that may never occur during behavior (e.g., high moments occur only after smaller moments, because moment builds up as the whisker bends against the object).

Curves depicting mean kinematic variables (ω, α, ζ, θ_{amp}, $\theta_{setpoint}$ and f_{whisk}) as a function of phase (Figures 7 and S5) were calculated as described above for phase tuning curves except after replacing the neural response with the kinematic variable. We used 30 bins to estimate probability distributions of ω, α, ζ, θ_{amp}, $\theta_{setpoint}$ and f_{whisk} (Figure S5A).

Data Analysis: Generalized Additive Models (GAMs)

We used statistical models to quantify the "instantaneous" (in 1 ms time bins) relationship between spike probability and various mechanical and kinematic variables. We used GAM statistical models because they offered improved performance over conventional Generalized Linear Models (GLMs; Figures S2A–S2D), yet preserve many of the advantages in interpretability that GLMs have over "black box" models such as Random Forests (Hastie et al., 2009; Wood, 2006). We fitted GAMs using the "mgcv" package in R (Wood, 2006), with a binomial error structure and logit link function. Each model was of the form:

$$logit(Y) = \sum_i f_i(X_i) + \epsilon$$

where Y is the expected spike probability in a 1 ms bin, and $f_i(X_i)$ is a smoothing spline of the i-th variable X_i, and ϵ is an error term. All variables were linearly interpolated from 500 samples/s (our high-speed video rate) to 1000 samples/s to match the binning of spikes. The smoothing for each spline was determined using a method (UBRE method in mgcv package; Wood, 2006) to prevent overfitting (values obtained with and without 10-fold cross validation of the entire model were nearly indistinguishable). Separate GAMs were fitted to contact (Figures 3 and S2) and whisking in air (Figure S6) data. To be included in fitting and prediction for a whisking in air GAM, a frame could not be an outlier (defined in "Glossary" subsection) for any of θ, ω, α, ζ. Similarly, to be included in a contact period GAM, a frame could not be an outlier for any of θ, ω, α, ζ, M_0, F_{ax}, F_{lat}, M_0', F_{ax}', or F_{lat}'. The goodness of fit was quantified using (1) Pearson correlation coefficient (r) between predicted spike probability and spike counts smoothed with a $\sigma = 4$ ms Gaussian kernel (in Figure S2 we show performance using kernels with $\sigma = 1$, 2, 4, 8, 16 or 32 ms), and (2) deviance, defined as -2 times the difference in log likelihood between the fitted model and a saturated model (with one data point per observation; Crawley, 2002). The "deviance explained" was 1 minus the ratio of model deviance to deviance of the null (one data point total) model. Deviance is a standard metric for quantifying and comparing the goodness of fit for linear models (Crawley, 2002), and unlike Pearson correlation does not require smoothing. We also fitted GLMs to the same data for contact periods (Figure S2). GLMs were fitted with 10-fold cross validation using the "GeneralizedLinearModel" class in MATLAB with a binomial error structure and logit link function.

Viscoelastic Model

We measured time series of bending moment ($M_0(t)$) and spike rate ($r_{spike}(t)$; in Hz) and formulated an empirical model of the intervening mechanics. We assume that M_0 resulting from whisker-object contact dominates viscoelastic stress such that strain can be a fixed function of M_0, and that the strain caused by M_0 saturates. First, a sigmoidal function transformed M_0 into strain:

$$\varepsilon(M_0) = \frac{2}{1 + exp(-k \cdot M_0 + C)} - 1 \qquad \text{(Eq. M1)}$$

where k (in (N-m)$^{-1}$) and C (unitless) are fitted parameters. Thus, ε ranges from -1 to $+1$ and can be thought of as a fractional change in displacement, $\Delta L/L_0$, where L measures displacement from a reference point in the follicle and L_0 is the starting value of L. The effect of non-zero C is to set a "resting" strain in the absence of contact, such that $\varepsilon \neq 0$ when $M_0 = 0$. We defined a "capped" version (ε_{spring}) of ε:

$$\varepsilon_{spring} = \begin{cases} \varepsilon_{lim}, & \varepsilon > \varepsilon_{lim} \\ -\varepsilon_{lim}, & \varepsilon < -\varepsilon_{lim} \\ \varepsilon, & otherwise \end{cases} \qquad \text{(Eq. M2)}$$

where ε_{lim} (unitless) is a fitted parameter. The quantities ε_{spring} and ε can be thought of as strain components dominated by elastic and viscous tissue interactions, respectively. The model is then in Kelvin-Voigt form:

$$\sigma = \sigma_{spring} + \sigma_{dashpot} = E \cdot \varepsilon_{spring} + \eta \cdot \frac{d\varepsilon}{dt} \tag{Eq. M3}$$

where total stress (σ; in Pa) is the sum of elastic (σ_{spring}) and viscous ($\sigma_{dashpot}$) stress, and E (in Pa) and η (in Pa-s) are fitted parameters that can be thought of as elastic and viscous moduli, respectively.

Finally, predicted spike rate ($\widehat{r}_{spike}$; in Hz) was simply a scaled version of σ, limited to the interval [0 Hz, 1,000 Hz].

$$\widehat{r}_{spike} = \begin{cases} 0 & \sigma \cdot q < 0 \\ 1,000 & \sigma \cdot q > 1,000 \\ \sigma \cdot q & \text{otherwise} \end{cases} \tag{Eq. M4}$$

The scale factor q (in Hz Pa^{-1}) was fixed for all units at 1,000.

The five parameters of the model (k, c, ε_{lim}, E, and η) were fitted to $M_0(t)$ after outlier removal, and after scaling M_0 by the inverse of the 80th percentile value of M_0 for each neuron (this scaling was absorbed by fitted parameter k). Fitting was performed (MATLAB "fmincon") by minimization of the squared error between r_{spike} and $\widehat{r}_{spike}$ evaluated for frames containing contact and whisking. The goal of the model was to explain spike rate during contact for Merkel and other SA afferents. In total, 25 of 26 (Merkel and unidentified SA) afferents were included (the fitting algorithm failed on 1 SA afferent; Table S1). Interestingly, the ratio of elastic to viscous stress in our fitted models was larger for afferents that preferred contacts in the retraction direction (not shown), perhaps due to asymmetric strains that result from deflections of a whisker in opposing directions (Whiteley et al., 2015). A prominent contribution of viscoelasticity to Merkel spiking would suggest that steady-state measurements of strain (Whiteley et al., 2015) in the Merkel-dense region of the follicle may represent a lower bound.

Histology: Trigeminal Ganglion

Mice were perfused intracardially with PBS followed by 4% paraformaldehyde in PBS (PFA). Tissue was post-fixed in 4% PFA overnight. Trigeminal ganglia (TG) were removed from the cranium and embedded in 5% agarose in PBS. Coronal sections (100 μm) were collected on a vibratome (Thermo Scientific, HM650V). Sections were washed in PBS then incubated at 4°C in PBT (1% bovine serum albumin and 0.4% Triton X-100 in PBS) for 1 hr. Cell bodies of TG neurons were labeled using rabbit anti-NeuN (Millipore, MABN140, 1:1000) followed by goat anti-rabbit Alexa Fluor 647 (ThermoFisher Scientific, A-21244, 1:500) in PBT. Sections were then washed in PBS and mounted in Vectashield with DAPI (Vector Laboratories, H-1200). Images were acquired using a CCD camera (QImaging, QIClick) on an epifluorescence microscope (Olympus, BX-41).

Histology: Whisker Pad

Mice were perfused and tissue post-fixed as described above. Whisker pads were dissected, depilated by chemical hair remover (Nair), and cryoprotected in 30% sucrose solution overnight. Pads were embedded in optimal cutting temperature solution (OCT, Tissue-Tek) and flash frozen at −80°C. Sections (100 μm) were collected on a cryostat (Leica). Sections were washed in PBS, incubated at 4°C in PBT for 1 hr, then stained using primary and secondary antibodies dissolved in PBT as follows. Merkel cells were labeled using rat anti-keratin 8 (Developmental Studies Hybridoma Data Bank, University of Iowa, TROMA-I, 2.5 μg/ml). Afferent endings expressing ChR2-YFP in $TrkC^{CreER};Rosa^{Ai32}$ were stained using rabbit anti-GFP (Millipore, AB3080, 1:500). Afferent endings expressing tdTomato in $TrkC^{CreER};Rosa^{Ai9}$ mice were stained using rabbit anti-RFP (Rockland, 600-401-379, 1:500). Secondary antibodies were goat anti-rat Alexa Fluor 647 (ThermoFisher Scientific, A-21247, 1:500) or goat anti-rabbit Alexa Fluor 488 (ThermoFisher Scientific, A-11008, 1:1000). Confocal images were acquired on an LSM 510 (Zeiss).

Histology: Quantification

To quantify specificity of labeling of whisker pad Merkel afferents (Figure S1B), we obtained confocal stacks from 3 whisker pads of 3 $TrkC^{CreER};Rosa^{Ai9}$ mice. We targeted for imaging all labeled afferent endings present in all macrovibrissae follicles in the 3 pads. This resulted in 472 confocal stacks obtained with a Zeiss Plan-Apochromat 20x 0.8 NA objective at a resolution of 512 pixels x 512 pixels, 0.82-1.16 μm/pixel, with 2-3 μm steps in the z axis. Two observers, working independently but not blinded to genotype, manually scored each labeled afferent into one of the following categories: (1) Merkel-cell associated; (2) longitudinal lanceolate; (3) club-like; (4) other ending type; (5) unclassified, given to afferents in which the ending type could not be determined. For afferents in which the observers did not agree, the category was set to (5), unclassified. Because we obtained confocal stacks from every labeled afferent we could find, without regard to whether it left the tissue section before terminating, was poorly stained, etc., many afferents (652 of 1,705) were scored as unclassified. Of these unclassified afferents, most (433 of 652) were due to disagreement between the two observers, almost always (412 of 433) because one observer scored the afferent as a Merkel and the other as unclassified. No afferents were scored as (4), other ending type. Merkel afferents were further scored by one observer as innervating the superficial Merkel cells in the rete ridge collar (51 or 1,045), or as innervating the deeper Merkel dense region (994 of 1,045).

Whisker and Other Hair Trimming

One day prior to electrophysiological recording, under isoflurane (1.5%) non-mystacial hairs on the left side of the face were trimmed short with fine forceps and microdissection scissors (Fine Science Tools). All whiskers and microvibrissae were trimmed short except β, γ, δ, B1-4, C1-4, and D1-4. For improved whisker tracking and improved follicle location estimates, we sought to minimize the hairs in the field of view that were not the whiskers of interest. We did not use chemical hair remover out of concern that it could compromise whisker mechanics. Thus, hair between the whiskers was manually removed by plucking. Non-whisker hairs were maintained at this short level by repeating this procedure as necessary.

Progressive Whisker Cutting Experiment

Trigeminal ganglion recordings were conducted as described earlier. The recording electrode was advanced by the micromanipulator until a well-isolated unit responsive to manual stimulation and active whisking was found. High-speed video was continuously recorded, including both active whisking periods and manual manipulations. While the whisker was at its full length, whisking in air (WIA) responses were recorded as the mouse actively whisked for several minutes. At the beginning of the experiment and following each manipulation, unit responses to manual touch were briefly recorded to enable online and post hoc matching of touch-evoked and whisking-evoked spike waveforms, thus ensuring correct mapping of the unit's receptive field. A sham handling manipulation, an internal control, was conducted to test the assumption that whisker handling did not affect WIA responses. The whisker shaft was held gently with Teflon-tipped forceps (Electron Microscopy Sciences) for several seconds and released. After sham handling and subsequent manipulations, the same unit's WIA responses were recorded for several minutes. For the first cut and subsequent cutting manipulations, the whisker was held with forceps, and a piece measuring approximately one third of its length was cut with microdissection scissors. The cut whisker fragment was collected in a plastic tube for post hoc measurement. For most experiments, this cutting, collection, and recording procedure was repeated for a second and third cut. After the final cut, the external length of the whisker was near zero. Any remaining external whisker length was measured immediately after the experiment with a microruler while the mouse was under isoflurane anesthesia.

Collected whisker fragments were transferred from the tube and arranged on a glass microscope slide. A glass coverslip was placed over the mounted whisker and fixed in place with nail polish. Brightfield images (BX-41 microscope, Olympus) of each fragment were obtained at high resolution (1 μm / pixel) using a CCD camera (QImaging, QIClick) and stitched together (FIJI; Preibisch et al., 2009). The lengths of each fragment were summed to find the total length of the intact whisker. The base radius (R; in m), total intact length (L; in m), and remaining length (x; in m) were used to estimate moment of inertia (I; in kg·m^2) of the whisker in the intact ($L = x$) and post-cut conditions ($L > x$) for subsequent analysis. The whisker was assumed to be an ideal, rigid cone rotating about an axis perpendicular to its long axis and located at the center of its base. I was estimated by the equation:

$$I = \pi \rho R^2 \left(\frac{1}{5L^2}x^5 - \frac{1}{2L}x^4 + \frac{1}{3}x^3 \right)$$

where whisker density (ρ) was assumed to be 2000 kg/m^3.

Sweeps with manual manipulations (touch, handling, cutting) were identified using high-speed video and removed from further analysis. The video recording session was partitioned into "cutting groups" that included all sweeps prior to any cutting or handling manipulation (*intact*), following sham handling (*sham*), and following each *n*-th cut (*Cut n*). Because the fully cut whisker could not be tracked, kinematic quantities were acquired from a surrogate whisker (described below). Spike waveforms were obtained and clustered across the entire session as described above. Units were included in further analyses if the shape and amplitude of the mean waveform of manual touch-evoked spikes did not change significantly over time and matched the mean waveform of whisking-evoked spikes (if any) for each cutting group.

Video Analysis

The backbone of each whisker was tracked at subpixel-resolution using the Janelia Whisker Tracker (Clack et al., 2012), yielding a set of "traces" (tracked objects in image X-Y coordinates) for each frame. All subsequent processing to extract θ, M_0, F_{ax}, F_{lat}, and the minimal distance from whisker to pole, d_{pole}, was conducted in MATLAB according to published methods (Pammer et al., 2013), with several modifications described below in "Video analysis" subsections. We used the Hilbert transform to quantify the instantaneous phase (Φ), amplitude (θ_{amp}) and setpoint ($\theta_{setpoint}$) of bandpass (8-30 Hz, Butterworth) filtered θ (Hill et al., 2011). Instantaneous whisking frequency (f_{whisk}) was calculated based on the time derivative of Φ after unwrapping and conversion to whisk cycles.

Video Analysis: Pre-processing

The location or absence of the pole was automatically determined for each video frame using a mean squared error based template matching algorithm. A number of events could render individual videos ineligible for further processing. These events included changes of pole position within a video, occasional failure of pole detection, grooming behavior, the experimenter introduced shadow of an optical fiber used for optogenetic stimulation, or whisker cutting manipulations. Individual trials were flagged by ad hoc heuristics as likely containing such events and marked for exclusion from further processing. Using a custom GUI, human curators manually inspected every trial and either verified the automatically determined status or, if necessary, corrected errors.

Video Analysis: Identifying Tracked Whiskers

To identify the same whiskers across frames we used a simple algorithm based on applying the following rules: (1) The location of the base $\vec{r}$ of a whisker trace in frame t, should have the smallest shift from $\vec{r}$ of the trace for the same whisker in the previous frame, t-1, among all candidate traces:

$$I_{interest}(t) = \underset{I_x(t-1)}{argmin} \left| \vec{r}_{I_{interest}(t)} - \vec{r}_{I_x(t-1)} \right|,$$

where $I_{interest}(t)$ is the identity label of the whisker of interest at frame t, $I_x(t-1)$ is the identity label of any trace x at frame t-1, $\vec{r}_{I(t)}$ represents the base location of a trace labeled by $I(t)$. (2) The shift of the base location of a trace should not exceed 40 pixels per frame (0.64 mm per ms). With this constraint, if a match could not be found in a certain frame, the frame was skipped and the program reported it as a missing measurement. Trials with more than 1% (25 frames) missing measurements were excluded from analysis. (3) The anterior-posterior order of the follicle positions of identified whiskers was not allowed to change. (4) Traces shorter than 100 pixels (3.4 mm) were ignored.

Video Analysis: Face Masking

Computing time series of whisker bending moment at the follicle (M_0) relies on being able to measure curvature from the same point on the whisker (arc length distance from the follicle) and to estimate the follicle location across all video frames. As previously described (Pammer et al., 2013), the use of a "mask" to truncate the tracked whisker traces as they approach the face helped prevent tracking "noise" near the face. The follicle location was then estimated by extrapolation along the angle of the whisker base past the intersection of the whisker and the mask (Pammer et al., 2013). In prior work (Pammer et al., 2013), a single mask was used per whisker across frames and trials. Here we extended this approach by using a separate mask for each frame, obtained using a custom algorithm that fitted a smoothing spline to the contour of the face. First, we subtracted from each frame a spatially scaled version of itself:

$$i_{diff}(x, y) = i(x, y) - i(1.2\, x, 1.2\, y),$$

where $i(x, y)$ and $i(1.2\, x, 1.2\, y)$ were pixel values at coordinate (x, y) and $(1.2\, x, 1.2\, y)$ in a video frame, respectively. The origin $(0, 0)$ was defined as the midpoint of the lower edge of the frame. Non-overlapping area between $i(x, y)$ and $i(1.2x, 1.2y)$ was excluded. The grayscale image i_{diff} was then converted to a binary image, b_{diff}:

$$b_{diff}(x, y) = \begin{cases} 0, & i_{diff}(x, y) < \frac{1}{2}\max(i_{diff}) \\ 1, & otherwise \end{cases}.$$

Because mice were head-fixed the face could appear only in a subset of pixels; the rest were set to 0:

$$b_{face}(x, y) = \begin{cases} 0, & y > 0.375\, x + 120 \\ b_{diff}(x, y), & otherwise \end{cases}.$$

A structural element 10 pixels wide and 1 pixel high was used (MATLAB "strel") to erode b_{face} (MATLAB "imerode") such that vertical structures were selectively removed.

A smoothing spline was fitted to points having pixel value 1 in the eroded b_{face} (MATLAB "fit"; smoothing parameter 1×10^{-5}). For faster computation, we reduced the smoothing spline to 10 equally spaced points (vectors) covering the segment of the face contour relevant for whiskers. The horizontal boundaries of this segment were determined for each frame by extending the minimal and maximal horizontal coordinates of identified whisker follicles by 30 pixels each. The resulting 10 vectors defining this segment were then scaled back by the factor of 1.2 used initially to compute i_{diff}.

We additionally applied a custom filter (across time) to handle rare occasions in which the mouse forepaw intruded into the image and caused sudden jumps in the fitted face contour. Taking the image x-coordinate of one point on the face contour at frame t, $x(t)$, as an example, the filter first obtained a "hypothesized" value of $x(t)$ as $x_{hypo}(t) = x(t-1)$. The initial estimate of $x(t)$ obtained from the process described above, $x_{initial}(t)$, was then combined with $x_{hypo}(t)$ to yield $x(t)$:

$$x(t) = k \cdot x_{hypo}(t) + (1 - k) \cdot x_{initial}(t),$$

$$k = \min\left(\left| x_{hypo}(t) - x_{initial}(t) \right|, \ 0.98\, R_x \right) / R_x,$$

where k sets the relative weighting of x_{hypo} and $x_{initial}$ in the estimate, and R_x is a constant that sets the maximal per-frame jump. R_x was set empirically to 0.64 mm. The maximum value of k was limited to 0.98 in order to avoid x getting trapped at $x(t) = x_{hypo}(t)$. For the first frame of each trial, x_{hypo} was set to the value of $x_{initial}$. Image y-coordinates were filtered identically except the constant limiting the maximal jump, R_y, was empirically set to 0.32 mm.

The mask for each frame was then obtained by scaling the face contour by a user-settable factor to offset it slightly from the face ($\sim$10-20 pixels). As in prior work (Pammer et al., 2013), frames in which the tracked whisker did not intersect the mask were

considered missing data. Thus, the user-settable factor was chosen to be as small as possible (to keep the mask as close as possible to the face) while also minimizing the number of frames without whisker-mask intersections.

Video Analysis: Whisker Baseline Curvature

Calculating change in whisker curvature at location p in time point t, ($\Delta\kappa_p(t)$, necessary to compute $M_0(t)$) depends on an estimate of the baseline curvature, $\kappa_p^{baseline}(t)$.

$$\Delta\kappa_p(t) = \kappa_p(t) - \kappa_p^{baseline}(t).$$

The $\kappa_p^{baseline}$ was derived from whisking-in-air curvature κ_p^{air}, i.e., in the absence of contact. However, when projected onto the video imaging plane, whisker curvature can appear to change due to roll of the whisker about its long axis (Knutsen et al., 2008) as well as to changes in elevation. To account for these variabilities, we used the following empirical model to estimate baseline for each time point:

$$\kappa_p^{baseline}(t) = f_{roll}(\theta(t)) + f_{elevation}(T),$$

where $f_{roll}(\theta(t))$ is a 2nd order polynomial fitted to $\kappa_p^{air}(t)$ as a function of θ across all trials and $f_{elevation}(T)$ is the median value of $\kappa_p^{air}(t) - f_{roll}(\theta(t))$ for each trial T (requires at least 50 frames, otherwise $f_{elevation}(T) = 0$ mm^{-1}). f_{roll} models the θ dependent variability in measured κ_p due to stereotyped protraction-dependent whisker roll (Knutsen et al., 2008). $f_{elevation}$ is a constant for each trial and models a slowly varying offset, presumably due to slow changes in whisker elevation. Finally, we calculated $\Delta\kappa_p$ for each time point as:

$$\Delta\kappa_p = \kappa_p - \kappa_p^{baseline}.$$

We estimated the effective "noise" level of our curvature estimates, σ_κ, for each session as:

$$\sigma_\kappa = 100\% \times \sum_i |\Delta\kappa_p(t_i)| \Big/ N_{air} \div \sum_j |\Delta\kappa_p(t_j)| \Big/ N_{contact},$$

where t_i are the N_{air} time points across the entire session where $d_{pole} > 1$ mm and $\theta_{amp} > 2.5°$, and t_j are the $N_{contact}$ time points containing whisker-pole contact. This quantifies how large curvature changes measured during whisking in air were as a percentage of those measured during contact. As an estimate of "noise," σ_κ is conservative in that this assumes curvature change during whisking in air results from measurement error, whereas to some extent it may also include true inertial bending (cf. Figure 6). Across 33 sessions, mean σ_κ was 7.8% ± 5.0% (±SD; Figure S7).

Video Analysis: Whisker Bending Stiffness

Bending moment at location p depends on change in curvature and bending stiffness, $M_p = \Delta\kappa_p(EI_p)$. The bending stiffness, EI_p, is the product of Young's Modulus (E) and the area moment of inertia at p, (I_p), a geometrical quantity (Birdwell et al., 2007; Pammer et al., 2013). Thus, in addition to uncertainty in $\Delta\kappa_p$ (quantified above), uncertainty in moment must consider E and I_p. We used a fixed value of $E = 5$ GPa, obtained in prior work for the mouse C2 whisker (Pammer et al., 2013) by comparison of force-displacement data to numerical simulations that model the whisker as a tapered beam (Birdwell et al., 2007). Stress-strain curves measured from distal and proximal segments of rat whiskers indicate that E varies among individual whiskers (standard deviation: ~1.5 GPa; Quist et al., 2011) and along the length of an individual whisker (~35%; Quist et al., 2011), but not systematically with whisker row/arc identity. Because I_p depends on the fourth power of whisker radius (Birdwell et al., 2007; Pammer et al., 2013), whisker geometry is the more consequential factor in determining bending stiffness for tapered whiskers. This geometry can vary considerably across individual whiskers, across mice, and even across time for individual mice. Here we obtained the individual whisker corresponding to every recorded neuron by plucking immediately following the recording session. This was particularly important for us because, in contrast to prior work that leveraged the stereotypy of whisker C2 (Pammer et al., 2013), we used several different whiskers. We mounted each plucked whisker on a glass slide and obtained high resolution (2.5 μm / pixel) brightfield images (BX-41 microscope, Olympus) covering the full length of the whisker using a CCD camera (QImaging, QIClick). Images were stitched together (FIJI; Preibisch et al., 2009), and the composite image was used to measure the whisker radius at points along its full length. We treated each whisker as a cone based on its radius at base and its length. Consistent with prior work (Hires et al., 2016), we found that the shape of individual whiskers deviated slightly from that of a pure cone (not shown), with uncertainty in I_p of ~50%. Taken together, our estimates of uncertainty in E, I_p and $\Delta\kappa_p$ imply that our reported values of absolute bending moment and forces must be considered approximations, accurate to no better than a factor of two (Taylor, 1997).

Video Analysis: Contact Detection

We classified frames into those with and without whisker-pole contact using a strategy that combined machine learning with manual curation. Classification was performed using Random Forests (using MATLAB "TreeBagger" class). The predictor vector $\vec{x}$ for the i-th time point t_i was:

$$\vec{x}(t_i) = \left(d_{pole}(t_{i-k}), d_{pole}'(t_{i-k}), \Delta\kappa_p(t_{i-k}), \Delta\kappa_p'(t_{i-k}) \right), \ k = -2, -1, 0, 1, 2$$

where d_{pole}' and $\Delta\kappa_p'$ are derivatives with respect to time. Missing data points in the predictors were interpolated. A separate classifier was trained for each session. Training data were based on videos curated by trained humans using a custom GUI. We manually curated the contact status of 1,837,500 frames, on average 55,682 frames per session. Classifier performance for each session was tested using out-of-bag prediction on all manually curated data for a session. The overall rate of correct classification was 99.5% ± 0.2% (mean ± SD across 33 sessions) with a false positive rate of 0.3% ± 0.1%. The rates at which a one frame (2 ms) shift occurred between the predicted and true times of contact onsets and offsets were 10.2% ± 4.8% and 12.4% ± 4.3%, respectively. These performance metrics used only frames during whisking ($\theta_{amp} > 2.5°$), since non-whisking periods were not used in any analysis that depended on contact classification. That is, our contact classification was intended to be valid only for periods of whisking.

Video Analysis: Smoothing and Differentiation

Trials with more than 2% of frames having missing θ, $\Delta\kappa_p$ or d_{pole} data were excluded. We first smoothed θ, M_0, F_{ax} and F_{lat} with a Savitzky-Golay filter (3rd order, span of 9 frames), interpolating missing frames when possible. Angular velocity, acceleration, and jerk were the first, second, and third derivatives of θ with respect to time, $\omega \equiv \theta'$, $\alpha \equiv \omega'$, and $\zeta \equiv \alpha'$, respectively. Derivatives were calculated using central differences (via MATLAB "gradient"; e.g., for frame i, $\omega(i) = (\theta(i+1) - \theta(i-1))/2)$. Derivatives for dynamic variables were $M_0' \equiv \Delta M_0 / \Delta t$, $F_{ax}' \equiv \Delta F_{ax} / \Delta t$, and $F_{lat}' \equiv \Delta F_{lat} / \Delta t$, where Δ indicates a difference from frame i to $i+1$. Variables were smoothed with a Savitzky-Golay filter (3rd order, span of 9 frames) after each differentiation step.

Video Analysis: Tracking "Surrogate" Whiskers

In three experimental conditions, we used surrogate whiskers because the whisker of interest could not be tracked. (1) When the whisker was cut progressively (Figure 6), after the final cut the whisker was too short to track. In order to maintain consistency of kinematic measurements across the sequential cuts, we tracked a "surrogate" whisker throughout the experiment, typically the most caudal remaining whisker. (2) Experiments in which the whisker of interest had been cut prior to start of recording (Figure 7F). In these cases, the surrogate whisker was from the same whisker arc as the whisker of interest. (3) We included two afferents in our analysis of phase tuning (Figures 5C–5E, S6, and 7G) obtained while multiple rows of whiskers were intact and occluded tracking of the whisker of interest. In these cases we typically tracked the most caudal whisker. For all data based on surrogate whiskers, only trials with no pole in reach of the whiskers were included, such that no contacts could occur.

Glossary

"Contact" periods: Frames with positive contact classification and $d_{pole} < 1$ mm.

"Whisking" periods: Frames with $\theta_{amp} > 2.5°$.

"Whisking in air" periods: Whisking frames with negative contact classification and $d_{pole} > 2$ mm.

"Non-whisking" periods: Frames with $\theta_{amp} < 1°$ that are not contact frames and $d_{pole} > 2$ mm.

"Touch-sensitive": Applies to a neuron with 95% confidence interval (CI) on mean spike rate during contact greater than and non-overlapping with both 95% CI for mean spike rate during non-whisking and 95% CI for mean spike rate during whisking in air.

"Whisking-sensitive": Applies to a neuron with 95% CI on mean spike rate during whisking in air non-overlapping with 95% CI for mean spike rate during non-whisking.

"T" neuron: Touch-sensitive but not whisking-sensitive.

"WT" neuron: Touch-sensitive and whisking-sensitive.

"WT*" neuron: WT neuron with mean spike rate > 1 Hz during whisking in air, and for which we collected at least 1,000 spikes (in order to calculate tuning surfaces, etc).

"Outliers": For M_0, F_{ax}, F_{lat}, M_0', F_{ax}' and F_{lat}', observations not between the 0.5 and 99.5 percentiles (i.e., 1% total were excluded). For θ, ω, α, ζ, θ_{amp}, f_{whisk}, $\theta_{setpoint}$, observations not between 0.25 and 99.75 percentiles. No outlier removal was performed on Φ.

QUANTIFICATION AND STATISTICAL ANALYSIS

Data analyses were conducted in MATLAB and R. Across experiments, we report analysis of simultaneous high-speed video and single-unit electrophysiological recordings from a total of n = 53 afferents, of which 17 were identified Merkels, 28 were unidentified SA afferents (likely Merkels), and 8 were RA. An additional 3 identified Merkels were used to characterize the optogenetic tagging method (Figure S1) but not otherwise analyzed (Table S1). We also report analysis of simultaneous high-speed video and EMG from 4 sessions total in 4 mice. We report analysis of high-speed video comprising 65,257,500 frames (2,175 min) total, including 25,365,000 frames (846 min) from identified Merkel afferents. Metadata and assignment to figure panels for all recordings is detailed in Table S1. Central tendency and dispersion measures are defined upon use in the text or figure legends. Sample sizes were not predetermined.

DATA AND SOFTWARE AVAILABILITY

Custom MATLAB and R code used for analyses and data will be made available upon reasonable request.